Thermodynamic Modeling of Aqueous Nanobubble Dispersion

Sofiane H. Achour[1], Tesleem Lawal[1], Kai Sheng[1], and Ryosuke Okuno[1]*

[1]Hildebrand Department of Petroleum and Geosystems Engineering, The University of Texas at Austin

Summary

The amount of gaseous species in water or brine can be greatly enhanced in the form of nanobubble (NB) dispersion. Aqueous NB dispersion has vast industrial applications, potentially in enhanced oil recovery (EOR) and carbon dioxide (CO_2) sequestration to control the mobility of gaseous species and the geochemistry associated with CO_2 dissolution. Development of such NB technologies depends on a proper understanding of thermodynamic properties of aqueous NB dispersion. The objectives of this research are to analyze the thermodynamic stability of aqueous NB dispersion and to apply a thermodynamic equilibrium model to analyze experimental data.

We first present a thermodynamic formulation for modeling aqueous NB dispersion, which clarifies that aqueous NB dispersion occurs in the aqueous phase that is supersaturated by the gaseous species in the system. That is, the gaseous species are present in two modes—dispersion of gas bubbles under capillary pressure and molecule dispersion (supersaturation) in the external aqueous phase. Such a thermodynamic system is referred to as aqueous NB fluid in this research and specified by (N_C + 3) variables (e.g., temperature, total volume, components' mole numbers, and capillary pressure), in which N_C is the number of components. We then present a novel implementation of the GERG-2008 equation of state (EOS) in minimization of the Helmholtz free energy to solve for equilibrium properties of aqueous NB fluid. GERG-2008 was used in this research because it is suitable for modeling an aqueous phase that is supersaturated by gaseous species.

The thermodynamic equilibrium model was applied to experimental data of aqueous NB fluid with nitrogen (N_2) at pressures up to 277 bara (4,019 psia) and 295.15 K (71.6°F). Application of the model to experimental data indicates that a large fraction (0.8–0.9) of the total amount of N_2 is in the form of molecule dispersion, but such supersaturation of the aqueous phase is possible because of the presence of NB dispersion with capillary pressure. That is, NB dispersion can increase the gas content in aqueous NB fluid by enabling gas supersaturation in the aqueous phase as a thermodynamic system.

Introduction

Many gaseous species, such as CO_2, H_2, N_2, and light hydrocarbons, are highly immiscible with water, and their equilibrium concentrations in aqueous fluids (water or brine) are often quite small under a wide range of conditions. However, various industrial processes can benefit if these immiscible gaseous species can be contained in the aqueous fluid as an effectively homogeneous phase, in which the external aqueous phase contains immiscible gas bubbles with a large number density.

There are many applications of gas bubbles in food, agriculture, wastewater treatment, mineral processing, pharmaceuticals, and other industries (Terasaka et al. 2021). However, these previous applications were limited primarily to atmospheric pressure, in which bubbled water is generated in an open system near atmospheric pressure (Kukizaki and Goto 2006). Such aqueous bubbles are not thermodynamically stable because the system is open, and they are not kinetically stable at a large number density without continuous addition of energy.

This paper is concerned with the development of NB technology that generates such aqueous fluids that can contain a large amount of an immiscible gas or gas mixture at elevated pressure in a controlled and scalable manner. The technology aims to make the gaseous species stably dispersed in the aqueous fluid as small bubbles, typically at a nanometer scale, and as dissolved molecules. These two modes (bubble dispersion and molecule dispersion) of containment can collectively make the overall concentration of the gaseous species greater than its inherent solubility in the aqueous fluid. Such aqueous fluid with gas-bubble/molecule dispersion is referred to as "aqueous NB fluid" in this paper.

As will be shown in this paper, aqueous NB fluid can be generated with a greater amount of the gaseous species at a higher pressure, and therefore, it finds more useful applications at elevated pressures. From the thermodynamic point of view, this is quite different from many papers addressing the question of a single bubble or multiple bubbles in an open system at low pressure (Iguchi et al. 1998; Kukizaki and Goto 2006; Ohgaki et al. 2010; Alheshibri et al. 2016; Azevedo et al. 2019; Ulatowski et al. 2019; Favvas et al. 2021; Zhou et al. 2021). However, no method had been found to control and design the physical and transport properties of such gas-containing fluids at high pressures, likely due to the lack of rigorous thermodynamic analysis and engineering tools for aqueous NB fluid.

High-pressure nonsubsurface processes that can benefit from the NB technology include CO_2 electrochemical reaction processes (Widiatmoko et al. 2021) and any other reactions that require a high concentration of gas species as reactants in aqueous reaction media. The technology can be used for high-pressure storage of gases, such as H_2, in tanks, pipes, and other pressure vessels. Some surface processes do not require the long-term stability of NB since they use the gaseous species for reactions (consumption).

Potential subsurface applications of the NB technology include EOR by gas injection and geological storage of gases in hydrocarbon reservoirs and aquifers (Li et al. 2023). In gas EOR, the injected gas not only flows through high-permeability layers and/or fracture networks but also gravity-segregates to the upper zones of the target reservoir. Such undesired flow regimes result in a rapid breakthrough of the injected gas into production wells, leading to inefficient volumetric sweep and costly recycling of the injection gas. To alleviate the problem, water-alternating-gas injection is commonly used; however, the water and gas may segregate, resulting in a loss of effectiveness. A low concentration of specially formulated surfactants can be added to the water so that a surfactant-stabilized gas foam bank is generated. With the high apparent viscosity of the foam phase, better mobility control of the gas injection is expected. However, two main

*Corresponding author; email: okuno@utexas.edu

This paper (SPE 215122) was accepted for presentation at the SPE Annual Technical Conference and Exhibition, San Antonio, Texas, USA, 16–18 October 2023, and revised for publication. Original manuscript received for review 19 October 2023. Revised manuscript received for review 27 January 2024. Paper peer approved 31 January 2024.

challenges of such gas foam technologies are (i) the stability of foam flowing in reservoir pores can be difficult to control and (ii) the use of surfactant adds to the complexity and cost of the field operations. Direct viscosification of CO_2 has been recently studied (Pal et al. 2022; Moortgat and Firoozabadi 2023; Guo et al. 2023).

The NB technology can effectively reduce the mobility of the injected gas because it flows with the external aqueous phase as the carrier. The apparent viscosity of such an aqueous NB fluid is shown to be slightly greater than the external phase alone with no NB. Therefore, the mobility of the gaseous species contained in aqueous NB fluid will be reduced substantially (by a factor of 10 in the experimental case with a Berea sandstone core) in comparison to two-phase slippage flow with relative permeabilities (Lawal et al. 2022). Also, the NB dispersion can substantially suppress the buoyant forces in comparison to when the gas is injected as a bulk gas phase in the presence of water (Ushikubo et al. 2010).

When the technology is applied for geological CO_2 sequestration, it can deliver a greater amount of CO_2 per volume of water for carbon mineralization in (ultra)mafic rocks (Snæbjörnsdóttir et al. 2020; Wang et al. 2023, 2024). Along with the mineralization, the reduced buoyant forces due to the containment of CO_2 as NB in the brine could mitigate the potential leakage of CO_2 to the surface through any hydraulic paths (faults and old wells). Many biogenic gas reservoirs can be used for CO_2 sequestration, but contamination of the reservoir gas by the injected CO_2 is a major concern. Using the NB technology, the mixing of CO_2 and natural gas (mainly methane) could be controlled by containing the CO_2 in the injected aqueous phase.

A theoretical understanding of aqueous NB fluid is crucial in developing NB technologies. We have developed software to perform thermodynamic calculations of fluid phases with curved interfaces, including gas bubbles in aqueous fluid (Achour and Okuno 2020, 2021). This paper presents the thermodynamic equilibrium model that enables a fundamental understanding of various factors affecting the properties of an aqueous NB fluid. In this paper, aqueous NB fluid is modeled as a thermodynamically stable state of a closed system, in which the external aqueous phase and the bubble phase coexist with no bulk gas phase for water and gaseous species.

Thermodynamic formulation of phase stability analysis has been established after Gibbs' original work, but there had been no rigorous solution to the phase stability problem in the presence of capillary pressure. Therefore, we made fundamental changes to the theoretical formulation by using the Helmholtz free energy instead of the Gibbs free energy for phase stability and equilibrium calculations under capillary pressure as detailed in Achour and Okuno (2020, 2021). In addition, modeling the properties of aqueous NB fluid requires an EOS that is capable of modeling water, a polar species. Furthermore, the external aqueous phase is supersaturated by gaseous species in aqueous NB fluid; hence, the EOS used for this research must be reliable in metastable regions of the energy hyperplane.

The GERG-2004 EOS was developed for the accurate prediction of thermodynamic properties of fluids (Kunz et al. 2007; Kunz and Wagner 2012). The EOS was calibrated for 18 species commonly present in natural gas, such as alkanes, water, and CO_2. The accuracy of the GERG-2004 EOS relied on a large fluid database from 650 experimental data sources, covering different types of thermodynamic properties, such as pressure/volume/temperature data, vapor-liquid equilibrium data, saturated liquid densities, and enthalpy changes. Then, the GERG-2008 EOS (Kunz and Wagner 2012) extended the GERG-2004 model to 21 species. The new model also extended the applicable conditions from 450 K to 700 K and from 35 MPa to 70 MPa, covering the vapor, liquid, supercritical, and multiphase regions. Varzandeh et al. (2017) showed that the GERG-2008 EOS is superior to cubic EOSs in terms of liquid density predictions over a wide range of temperature and pressure conditions. Kontogeorgis and Folas (2009) gave comprehensive descriptions regarding the applications of cubic EOSs for various fluids, including polar species.

The formulation of GERG-2008 takes an explicit form of reduced Helmholtz free energy as a function of reduced temperature, reduced density, and composition, which facilitates the thermodynamic computations based on the minimization of the Helmholtz free energy (Achour and Okuno 2020, 2021). Also, Aursand et al. (2016) compared the GERG-2008 EOS with other EOSs in their ability to reproduce spinodal limits and metastable zones for pure components. They discovered that GERG-2008 is more accurate than other Helmholtz-based EOSs, such as PC-SAFT EOS, in metastable zones. In this research, therefore, the GERG-2008 EOS is adopted for the phase equilibrium calculation of aqueous NB fluids.

There are a few challenges in applying the GERG-2008 EOS for modeling aqueous NB fluids. According to Gernert and Span (2016), GERG-2008 is not quite accurate for phase-boundary predictions for CO_2-containing mixtures and gas solubility in water. As will be shown in this paper, the residual part of the reduced Helmholtz free energy consists of two parts—a linear combination of residual parts for each component in the mixture and a departure function, in GERG-2008. The departure function was only calibrated for seven hydrocarbon binaries. Gernert and Span (2016) improved the matching for water/CO_2 mixtures by calibrating the departure-related coefficients. We revisited their modifications in terms of departure functions and have improved the accuracy of GERG-2008 for water/N_2 mixtures.

Also, the determination of the right compressibility factor is more challenging with GERG-2008 than with cubic EOSs. GERG-2008 can have more than three roots and no analytical solution exists for the root-finding problem. We found in this research that commercial codes, such as REFPROP (Lemmon et al. 2017, 2018), may cause convergence issues because of their erroneous compressibility factor. We have developed a more robust algorithm for compressibility factor with GERG-2008.

This paper first presents the formulation and algorithms for computing the properties of aqueous NB fluids using the GERG-2008 EOS. The model is then used to match and analyze the experimental data of aqueous NB fluid with N_2. To the best of our knowledge, this is the first time aqueous NB fluids are modeled using rigorous thermodynamic principles with a quantitatively reliable EOS, GERG-2008.

Formulation

This section presents the formulation for computing the equilibrium properties of aqueous NB fluid at given thermodynamic conditions (e.g., component mole numbers, temperature, volume, and external phase pressure) assuming a uniform size of bubbles. Note that this research is concentrated on the modeling of aqueous NB fluid as a two-phase equilibrium system in which NBs are dispersed in the external aqueous phase that is supersaturated by the gaseous species under capillary pressure in a closed system. This research does not deal with the onset of bubble nucleation and the dynamics of incipient bubbles, which are discussed elsewhere (e.g., Ono and Kondo 1960; Firoozabadi 2016; Jin et al. 2020). Firoozabadi (2016) gives comprehensive derivations of bubble nucleation using the Gibbs free energy.

Thermodynamic Stability and Equilibrium of Aqueous NB Fluid. Achour and Okuno (2020, 2021) presented that phase equilibrium with capillary pressure is naturally modeled by the minimization of the Helmholtz free energy. The iterative solution to a phase equilibrium problem using an EOS is quite nonlinear, but using the Helmholtz free energy involves only one energy surface, unlike the conventional method of using the Gibbs free energy, regardless of the number of phases with capillary pressure. Pressures for different equilibrium phases (i.e., capillary pressure) were inherently modeled as part of the minimization of the Helmholtz free energy. This subsection briefly reviews the formulation of Achour and Okuno (2020, 2021) and also gives equilibrium properties of aqueous NB fluid.

A closed system at a fixed temperature T, total volume V_{total}, and total mole numbers n_i (i = 1, 2, …, N_C) of N_C components is at an equilibrium state when the Helmholtz free energy of the system cannot be reduced for any possible perturbation. That is, the system is stable if

$$\mathrm{d}A_{\text{total}} = \mathrm{d}A_V + \mathrm{d}A_\sigma + \mathrm{d}A_L \geq 0, \tag{1}$$

for any perturbation of thermodynamic variables. In the above equation, $\mathrm{d}A_{\text{total}}$, $\mathrm{d}A_V$, $\mathrm{d}A_\sigma$, and $\mathrm{d}A_L$, respectively, represent the change in the Helmholtz free energy for the system, the vapor phase, the interface, and the liquid phase. The changes in the Helmholtz free energy for the V- and L-phases are

$$\mathrm{d}A_V = -S_V \mathrm{d}T_V - P_V \mathrm{d}V_V + \sum_{i=1}^{N_C} \overline{G}_{iV} \mathrm{d}n_{iV}, \tag{2}$$

$$\mathrm{d}A_L = -S_L \mathrm{d}T_L - P_L \mathrm{d}V_L + \sum_{i=1}^{N_C} \overline{G}_{iL} \mathrm{d}n_{iL}, \tag{3}$$

and the change in the Helmholtz free energy for the interface is

$$\mathrm{d}A_\sigma = -S_\sigma \mathrm{d}T_\sigma - P_\sigma \mathrm{d}V_\sigma + \sum_{i=1}^{N_C} \overline{G}_{i\sigma} \mathrm{d}n_{i\sigma} + \sigma \mathrm{d}a. \tag{4}$$

In the above equations, S is the entropy, T is the temperature, P is the pressure, V is the volume, $\overline{G}_i$ is the partial molar Gibbs free energy of component i, σ is the interfacial tension (IFT) between the V- and L-phases, a is the interfacial area, n_i is the mole number of component i, and N_C is the number of components. Note again that this research deals with aqueous NB fluid as a two-phase equilibrium system as evident from Eqs. 2 and 3, in which the two phases are given different pressures unlike the formulation of gas-bubble nucleation in Ono and Kondo (1960) and Firoozabadi (2016).

The thermodynamic specifications of T, V_{total}, and n_i require

$$\mathrm{d}n_{iV} + \mathrm{d}n_{i\sigma} + \mathrm{d}n_{iL} = 0, \tag{5}$$

$$\mathrm{d}V_V + \mathrm{d}V_\sigma + \mathrm{d}V_L = 0, \tag{6}$$

$$\mathrm{d}T_V = \mathrm{d}T_\sigma = \mathrm{d}T_L = 0. \tag{7}$$

These conditions yield

$$\mathrm{d}A_{\text{total}} = -\left(P_V - P_L\right)\mathrm{d}V_V - \left(P_\sigma - P_L\right)\mathrm{d}V_\sigma + \sum_{i=1}^{N_C}\left(\overline{G}_{iV} - \overline{G}_{iL}\right)\mathrm{d}n_{iV} + \sum_{i=1}^{N_C}\left(\overline{G}_{i\sigma} - \overline{G}_{iL}\right)\mathrm{d}n_{i\sigma} + \sigma\,\mathrm{d}a. \tag{8}$$

Because $\mathrm{d}V_\sigma$ and $\mathrm{d}n_{i\sigma}$ are relatively small, the second and fourth terms are negligible in comparison to the other terms on the right-hand side of the above equation. Then,

$$\mathrm{d}A_{\text{total}} = -\left(P_V - P_L\right)\mathrm{d}V_V + \sum_{i=1}^{N_C}\left(\overline{G}_{iV} - \overline{G}_{iL}\right)\mathrm{d}n_{iV} + \sigma\,\mathrm{d}a. \tag{9}$$

$\mathrm{d}A_{\text{total}}$ tends to zero with diminishing net mass transfer between the V- and L-phases, that is,

$$\overline{G}_{iV} - \overline{G}_{iL} = 0. \tag{10}$$

$\mathrm{d}A_{\text{total}} = 0$ and Eq. 10 require the following condition:

$$\left(P_V - P_L\right)\mathrm{d}V_V = \sigma\,\mathrm{d}a \;\text{ or }\; P_V - P_L = \sigma\,\mathrm{d}a/\mathrm{d}V_V. \tag{11}$$

Then, Eqs. 10 and 11 define the first-order necessary conditions for the Helmholtz free energy to be a minimum at a given T, V_{total}, and n_i (i = 1, 2, …, N_C). Note that Eq. 11 holds for equilibrium phases as also emphasized in Achour and Okuno (2020).

The minimization of the Helmholtz free energy is subject to the molar volume constraint

$$\underline{V}_j > \underline{V}_{\lim j}, \tag{12}$$

where for the L- and V-phases ($j = V$ or L) and the positivity of mole numbers

$$n_{ij} > 0, \tag{13}$$

where i = 1, 2, …., N_C and $j = V$ or L. In Eq. 12, $\underline{V}_{\lim j}$ represents the smallest possible molar volume by the EOS used. For cubic EOSs [e.g., the Peng-Robinson (PR) EOS (Robinson and Peng 1978)], $\underline{V}_{\lim j}$ is the covolume parameter (Achour and Okuno 2021).

Eq. 9 or Eq. 11 clarifies that the interfacial area a gives a state variable ($P_V - P_L$) for thermodynamic aqueous NB fluid, which is constant at zero for the phase equilibrium state with a planar interface between fluid phases. Assuming a uniform radius r of N_b bubbles for V_V at equilibrium,

$$V_V = 4\pi r^3 N_b/3, \tag{14}$$

and the total surface area a is

$$a = 4\pi r^2 N_b. \tag{15}$$

Using Eqs. 14 and 15, the capillary pressure P_C (= $P_V - P_L$) is

$$P_C = \sigma \mathrm{d}a/\mathrm{d}V_V = 2\sigma/r. \tag{16}$$

Note that in Eq. 16, P_C depends on r assuming the V-phase is a cluster of spherical bubbles with a uniform radius r. Therefore, it is possible to specify a value for P_C by specifying r and a values or a function for σ in addition to T, V_{total}, and n_i (i = 1, 2, …., N_C) (Achour and Okuno 2020). For a given equilibrium solution, the number of bubbles N_b can be calculated by using Eq. 14.

The problem of thermodynamic aqueous NB fluid given above is solved by using the GERG-2008 EOS in this paper. The existence of a thermodynamically valid solution using such a quantitatively accurate EOS indicates the feasibility or stability of individual NB in the aqueous phase that is supersaturated by the gaseous species. Note that the multibody stability of NB cannot be analyzed in the above thermodynamic framework, and perhaps detailed experiments are crucial at the current stage of research.

Spontaneity Analysis Using the Helmholtz Free Energy. When aqueous NB fluid is formed from a mixture of water and gaseous species using a certain device, a sufficient amount of energy must be available to cause the interfacial area for the bubbles in the external water phase in the system at equilibrium (Weijs et al. 2012). When such a system is set at a given temperature and total volume, the total Helmholtz free energy of the mixture is reduced to that of an aqueous NB fluid consisting of two phases (the external water phase and gas bubbles). This reduction in the Helmholtz free energy ΔA_{total} must be greater than the total Helmholtz free energy for the interface. This is a theoretical thought process without specifying the process of generating such aqueous NB fluid; therefore, the spontaneity analysis given in this section is less strict than the requirement in actual processes. For example, any dissipation will demand an additional amount of energy beyond the theoretically required amount of energy.

The Helmholtz free energy for the original mixture is A_I and that for aqueous NB fluid is ($A_V + A_\sigma + A_L$). For the latter state to be thermodynamically more stable than the former, $A_I > (A_V + A_\sigma + A_L)$ or

$$A_I - \left(A_V + A_L\right) > A_\sigma = \sigma a, \tag{17}$$

assuming the mole numbers of components and the volume for the interface are small so that $A_\sigma = G_\sigma - P_\sigma V_\sigma + \sigma a$ can be approximated to be $A_\sigma = \sigma a$. The total volume of the system V_{total} is common for the initial and the final (equilibrium) states. Dividing Eq. 17 by $V_{\text{total}}RT$, we have

$$A_{RI} - \left(A_{RV} S_V + A_{RL} S_L\right) > \varepsilon, \tag{18}$$

where $A_{RI} = A_I/V_{\text{total}}RT$, $A_{RV} = A_V/V_V RT$, $A_{RL} = A_L/V_L RT$, $S_V = V_V/V_{\text{total}}$, $S_L = V_L/V_{\text{total}}$, and $\varepsilon = \sigma a/V_{\text{total}}RT$. A_{RI} is the reduced Helmholtz free energy density at the initial state (hypothetically single phase); A_{Rj} is the reduced Helmholtz free energy density for phase j; S_j is the equilibrium volumetric fraction (i.e., saturation) for phase j; and R is the universal gas constant.

The material balance for component i

$$n_i = n_{iV} + n_{iL}, \tag{19}$$

can be expressed as

$$d_i = s d_{iV} + \left(1 - s\right) d_{iL}, \tag{20}$$

where $d_i = n_i/V_{\text{total}}$, $d_{iV} = n_{iV}/V_V$, and $d_{iL} = n_{iL}/V_L$. We use s in place of S_V for analyzing the spontaneity criterion (Eq. 18) in s space. That is, if

$$D\left(s\right) = A_{RI}\left(s\right) - \left[s\, A_{RV} + \left(1 - s\right) A_{RL}\right] > \varepsilon, \tag{21}$$

then aqueous NB fluid has a smaller Helmholtz free energy than the hypothetically single phase for the specified temperature, total volume, and mole numbers of components.

The D function is nonlinear with s, while ε increases linearly with s with a slope of $3\sigma/rRT$ because $\varepsilon = 3\sigma s/rRT$. Note that at $s = 0$, $D = \varepsilon = 0$. Therefore, $D > \varepsilon$ for a small value of s if the gradient of D with respect to s is greater than $3\sigma/rRT$. The gradient of D is

$$\frac{\partial D}{\partial s} = \sum_{i=1}^{N_C} \left(\ln f_i\left(s\right) - \ln f_i\left(s = 0\right)\right)\left(d_{iV} - d_{iL}\right) + \frac{P_V - P_L}{RT}, \tag{22}$$

where the Gibbs-Duhem equation was used. At $s = 0$, the gradient becomes $(P_V - P_L)/RT$. Then, the nucleation of bubbles for a small value of s is likely spontaneous if

$$P_V - P_L - 3\sigma/r > 0. \tag{23}$$

Eq. 23 cannot be met if $P_V - P_L = 2\sigma/r$ (see Eq. 16) as in the current thermodynamic analysis. Note that Eq. 23 is similar to the widely used expression for the nucleation energy barrier (Kaptay 2012). The criterion (Eq. 23) may be temporarily satisfied upon gas nucleation, but such bubbles may not be thermodynamically stable unless the more fundamental criterion (Eq. 21) is satisfied at equilibrium. This analysis indicates that the thermodynamic stability of aqueous NB fluid requires a minimum amount of gaseous species in the system so that the criterion shown by Eq. 21 can be met. This highlights the importance of supersaturation of the aqueous phase by gaseous species for generation of aqueous NB fluid.

Thermodynamic Models

This section presents the thermodynamic models used for estimating properties of aqueous NB fluid at given experimental conditions assuming a uniform size of bubbles. The first part is focused on the GERG-2008 EOS and the second part on the IFT model used in this research.

Equation of State. One challenge in accurately modeling multiphase behavior including capillary pressure is that the equilibrium phase of lower pressure lies on the metastable part of the free energy surface. This part of the free energy lies outside the traditional range of thermodynamic variables used for calibrating the EOS. As a result, most EOSs are uncertain about the accuracy of modeling metastable phases (Aursand et al. 2016). The GERG-2008 EOS is relatively accurate in modeling metastable phases (Imre et al. 2013; Aursand et al. 2016). This is the main reason why this research used the GERG-2008 EOS. The comparison of different EOSs for modeling aqueous NB fluids is outside of the scope of this research. Nonetheless, Appendix A illustrates the widely known challenges of a cubic EOS in matching solubilities for water-gas mixtures. If inherent solubilities (without capillary pressure) are not matched, the EOS cannot be reliable in metastable zones.

The GERG-2008 EOS (Kunz and Wagner 2012) is a multiparametric EOS and gives the Helmholtz free energy as a function of composition, temperature, and molar density. Kunz and Wagner (2012) and Kunz et al. (2007) gave derivatives for this EOS. This section presents the equations for the Helmholtz free energy as given by the GERG-2008 EOS. The analytical expression for other thermodynamic variables, such as pressure and fugacity, are given in Achour (2023). The EOS in a dimensionless form is

$$\alpha\left(\delta,\tau,\mathbf{x}\right)=\frac{\underline{A}}{RT}=\alpha^{0}\left(\underline{d},T,\mathbf{x}\right)+\alpha^{r}\left(\delta,\tau,\mathbf{x}\right), \tag{24}$$

where δ is the reduced density,

$$\delta=\underline{d}/\underline{d}_{r}\left(\mathbf{x}\right), \tag{25}$$

τ is the inverse of reduced temperature,

$$\tau=T_{r}\left(\mathbf{x}\right)/T, \tag{26}$$

α^{0} represents the contribution from the ideal gas mixture using $\underline{d}$, T, and $\mathbf{x}$, and α^{r} represents the residual mixing behavior using δ, τ, and $\mathbf{x}$. In Eqs. 24 and 25, $\underline{d}_{r}$ and T_{r} are the reducing molar density and temperature defined as

$$\frac{1}{\underline{d}_{r}}=\sum_{i=1}^{N_C}\frac{x_i^2}{\underline{d}_{ci}}+\frac{1}{4}\sum_{i=1}^{N_C-1}\sum_{j=i+1}^{N_C}x_i x_j\beta_{vij}\gamma_{vij}\frac{x_i+x_j}{\beta_{vij}^2 x_i+x_j}\left(\frac{1}{\underline{d}_{ci}^{\frac{1}{3}}}+\frac{1}{\underline{d}_{cj}^{\frac{1}{3}}}\right)^3, \tag{27}$$

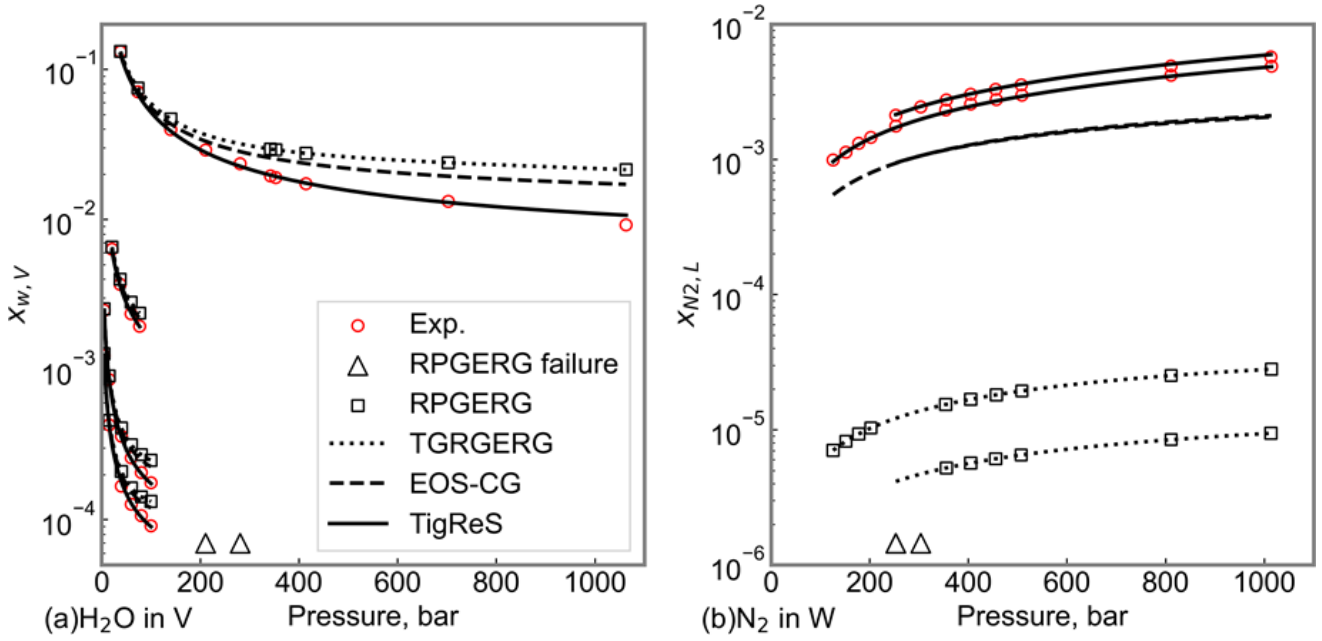

Fig. 1—Equilibrium mole fractions of water in the vapor phase and nitrogen in the aqueous phase; (a) shows water mole fractions in the vapor phase at 273.15 K, 283.15 K (Oellrich and Althaus 2004), 323.15 K (Rigby and Prausnitz 1968), and 422.4 K (Tabasinejad et al. 2011) from bottom to top; (b) shows nitrogen mole fractions in the aqueous phase at 323.15 K and 298.15 K (Maslennikova 1971) from bottom to top . The hollow squares and the dotted lines, respectively, show the equilibrium mole fractions calculated using REFPROP (RPGERG) and the in-house implementation of GERG (TGRGERG). The dashed lines show the equilibrium mole fractions using the EOS-CG calibration of GERG parameters (Gernert and Span 2016). The solid lines show the calibrated GERG model (TigReS), for which the tuned parameters are shown in Tables 1 and 2.

	β_{vij}	β_{Tij}	γ_{vij}	γ_{Tij}
N_2/H_2O	1.058714	1.130886	0.9284938	0.8703639

Table 1—Binary parameters for reducing parameter functions for density and temperature.

Binary Pair	k	$d_{ij,k}$	$t_{ij,k}$	$n_{ij,k}$	F_{ij}
N_2/H_2O	1	1	1.0	1.872926	1.0
	2	1	1.55	−1.830299	

Table 2—Coefficients and exponents for binary departure functions α_{ij}^r. The N_2/H_2O binary pair is calibrated by minimizing the residuals using Scipy's implementation of the Nelder-Mead algorithm.

and

$$T_r = \sum_{i=1}^{N_C} x_i^2 T_{ci} + \sum_{i=1}^{N_C-1} \sum_{j=i+1}^{N_C} 2x_i x_j \beta_{Tij} \gamma_{Tij} \frac{x_i + x_j}{\beta_{Tij}^2 x_i + x_j} \sqrt{T_{ci} T_{cj}}, \quad (28)$$

where β_{vij}, γ_{vij}, β_{Tij}, and γ_{Tij} are calibration parameters that can be adjusted to match the experimental data. The code for the GERG-2008 EOS was developed by converting the FORTRAN77 code from Lemmon et al. (2017) to a modern FORTRAN (FORTRAN2003) and by adding the missing routines for derivatives of pressure with mole number, logarithm of fugacity, and derivatives of the logarithm of fugacity.

Kunz and Wagner (2012) calibrated the parameters β_{vij}, γ_{vij}, β_{Tij}, and γ_{Tij} for the reduced temperature, molar density, and residual component for the Helmholtz free energy of water/gas systems. However, Kunz and Wagner (2012) did not use enough data to accurately calibrate the binary departure parameters for mixtures of water and gases, such as nitrogen (N_2) and carbon dioxide (CO_2). Gernert and Span (2016) calibrated the binary departure EOS for mixtures of water with various gases including N_2 and CO_2 as presented for various applications (Tabasinejad et al. 2011; Jarrahian and Nakhaee 2019; Heidaryan et al. 2019; Trædal et al. 2021). Additional details and derivatives of the GERG-2008 EOS are given in Kunz et al. (2007).

Fig. 1 shows experimentally measured and calculated values using different calibrations of the GERG-2008 EOS for the equilibrium water/N_2 mole fractions in the liquid and vapor phases at different temperatures and pressures. **Fig. 1a** shows the mole fraction of water in the vapor phase and **Fig. 1b** shows the mole fraction of N_2 in the liquid phase.

The REFPROP software developed by the National Institute for Science and Technology computes thermodynamic properties using various EOS (Lemmon et al. 2018). It includes liquid-vapor flash calculations using the GERG-2008 EOS. The hollow squares in **Fig. 1** are the results of using REFPROP. The dotted lines show the equilibrium mole fractions computed by our implementation of the GERG-2008 EOS, which match the REFPROP values. The hollow triangles show the pressure values at which the flash calculation of REFPROP failed. The GERG-2008 EOS as implemented in this research converged to the correct solution at all pressures. This demonstrates the improved robustness of the flash calculation algorithm used in this paper.

The dashed lines represent the equilibrium mole fractions computed by the EOS-CG calibration of GERG parameters (Gernert and Span 2016). For water/N_2, neither GERG nor EOS-CG match the data well. Therefore, the GERG parameters need to be recalibrated to match the data. Recalibrated GERG parameters ("TigReS" in **Fig. 1**) are shown in **Tables 1 and 2**. We observed in this research that the multiparametric nature of the GERG-2008 EOS allowed for the flexibility that enabled the accurate modeling of water/N_2 mixtures (involving polarity) as implemented in an in-house compositional flow simulator TigReS. This was not the case with the traditional cubic EOS (e.g., the PR EOS) as shown in Appendix A. However, we expect that other EOSs (e.g., cubic-plus-associate EOS) can also be used with the presented formulation for aqueous NB fluid if it is capable of modeling metastable regions of the energy hyperplane for the aqueous phase.

One disadvantage of the multiparametric GERG-2008 EOS is that it does not explicitly give an expression for the covolume parameter, which is used in the algorithms (Achour and Okuno 2020, 2021) to compute the physical limits of the molar volume as constrained by Eq. 12. Models were developed for pseudo-covolume parameters to match the molar volume that yields a pressure prediction of 2×10^7 bar; that is, $b = \underline{V}\left(P = 2 \times 10^7 \text{ bar}\right)$.

First, the pseudo-covolume values for pure N_2 and water were determined based on the GERG-2008 EOS, as calibrated by Kunz and Wagner (2012) and given in **Table 3.**

	N_2	H_2O
b (cm^3/mol)	5.41358	4.83885

Table 3—Pseudo-covolume for pure substances based on GERG-2008.

Then, two models were calibrated to covolumes of water/N_2 mixtures. The first model uses a geometrical average like the van der Waals mixing rule for the attraction parameter

$$b(\mathbf{x}) = \sum_{i=1}^{N_C}\sum_{j=1}^{N_C}\sqrt{b_i b_j}x_i x_J(1-k_{ij}), \tag{29}$$

where k_{ij} is a binary interaction parameter (BIP) for the binary pair of components i and j. The second model uses the mixing rule for the reducing density mixing rule from the GERG-2008 EOS:

$$b\left(\mathbf{x}\right) = \sum_{i=1}^{N_C} x_i^2 b_i + \sum_{i=1}^{N_C-1}\sum_{j=i+1}^{N_C} c_{b,ij} f_{b,ij}, \tag{30}$$

where

$$c_{b,ij} = 2\beta_{b,ij}\gamma_{b,ij}b_{ij}, \tag{31}$$

$$f_{b,ij} = x_i x_j \frac{x_i + x_j}{\beta_{b,ij}^2 x_i + x_j}, \tag{32}$$

$$b_{ij} = \frac{1}{8}\left(b_i^{\frac{1}{3}} + b_j^{\frac{1}{3}}\right)^3. \tag{33}$$

$\beta_{b,ij}$ and $\gamma_{b,ij}$ are calibration parameters. **Fig. 2** compares the pseudo-covolume parameter values calculated by the definitions above. **Tables 4 to 7** show the pure substance covolumes and the calibrated parameters for both models.

	N_2	H_2O
b (cm^3/mol)	5.41358	4.83885

Table 4—Covolume for pure substances.

	N_2	H_2O
N_2	0	–0.2234
H_2O	–0.2234	0

Table 5—Optimal BIP values k_{ij} for the geometrical average.

	N_2	H_2O
N_2	0	1.0023
H_2O	1.0023	0

Table 6—Covolume parameter $\beta_{b,ij}$ for the GERG-type mixing rule.

	N_2	H_2O
N_2	0	1.2212
H_2O	1.2212	0

Table 7—Covolume parameter $\gamma_{b,ij}$ for the GERG-type mixing rule.

IFT for Water and N_2. Eq. 11 is one of the main equations solved by the phase-split calculation algorithm for the equilibrium properties of aqueous NB fluid in this research. This equation is given by the pressure modeled by an EOS and the capillary pressure for a given r. The equilibrium IFT is generally a function of the equilibrium phase compositions, L and V, where the L-phase is in a metastable region of the free energy hypersurface. This subsection presents the development of an IFT model for water/N_2 NBs that accounts for the L-phase composition and density in the metastable region.

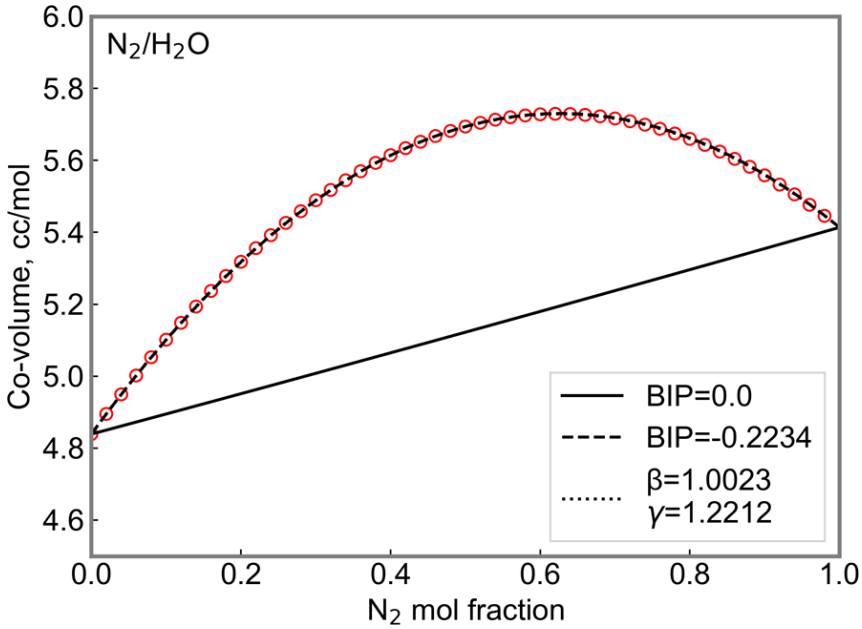

Fig. 2—Calibrated pseudo-covolume for water/N_2. The hollow red circles show the molar volume root for a pressure of 2×10^7 bar. The dashed and bold lines, respectively, show the matched covolume using the geometrical mixing rule and the reference mixing rule for a BIP of zero. The dotted line represents the matched pseudo-covolume using the GERG-type mixing rule, and it overlaps with the dashed line.

The IFT is a function of the radius of curvature (Ono and Kondo 1960; Firoozabadi 2016), the excess composition of the interface, and the composition of the two phases that the interface separates (Schechter and Guo 1998). The model presented in this section neglects the first two effects and focuses mostly on the effect of the L-phase and V-phase compositions on the IFT.

The IFT was calibrated based on the data by Yan et al. (2001) on water/N_2 interfaces with large curvatures such that the effect of curvature on the IFT is negligible. The model calibrated to fit the experimental data is a modified Parachor model

$$\sigma = \left(\chi \sum_{i=1}^{N_C} \Pi_i \left(d_{iL} - d_{iV} \right) \right)^{\gamma}, \tag{34}$$

where χ is a temperature-dependent coefficient. This modification can be implemented by simply changing the values of Π_i in the input file to $\chi\Pi_i$. The calculated IFT and experimentally measured values are shown in **Fig. 3** using solid lines and hollow symbols at various temperatures and pressures. **Table 8** shows the Parachor coefficients and calibrated Parachor exponent. **Fig. 4** shows the χ parameter values for different temperatures, which can be linearly correlated as

γ	0.7
Π_{N_2}	61.12
Π_{H_2O}	51.0

Table 8—Parachor coefficients for water (Fechter et al. 2023), N_2 (Schechter and Guo 1998), and Parachor exponent.

$$\chi = -0.5191 \left(T - 273.15 \right) + 173.2. \tag{35}$$

Algorithms

This section presents a concise description of the flash calculation algorithm for a given composition and total molar volume (Achour and Okuno 2020, 2021; Achour 2023) and two important developments that were necessary to implement the GERG-2008 EOS in minimization of the Helmholtz free energy. These models and algorithms include a correlation for the pseudo-covolume parameter for gas-water mixtures and a new procedure for estimating the initial guess for stability analysis and phase-split calculations.

Flash Calculation. The algorithm uses the successive substitution (SS) method followed by a Newton-Raphson (NR) algorithm. SS is based on the Mikyška and Firoozabadi (2011) adaptation of the Michelsen (1982) algorithm for minimization of the Helmholtz free energy. The algorithm used here was first published by Achour and Okuno (2021), and details of its improved version can be found in Achour (2023). The switch from SS to NR occurs when the criterion $\max_{i<N_C+1} \left\{ \left| F_i \right| \right\} < \varepsilon_{NR}$ is met, where F_i for $i = 1,\ldots N_C$ is

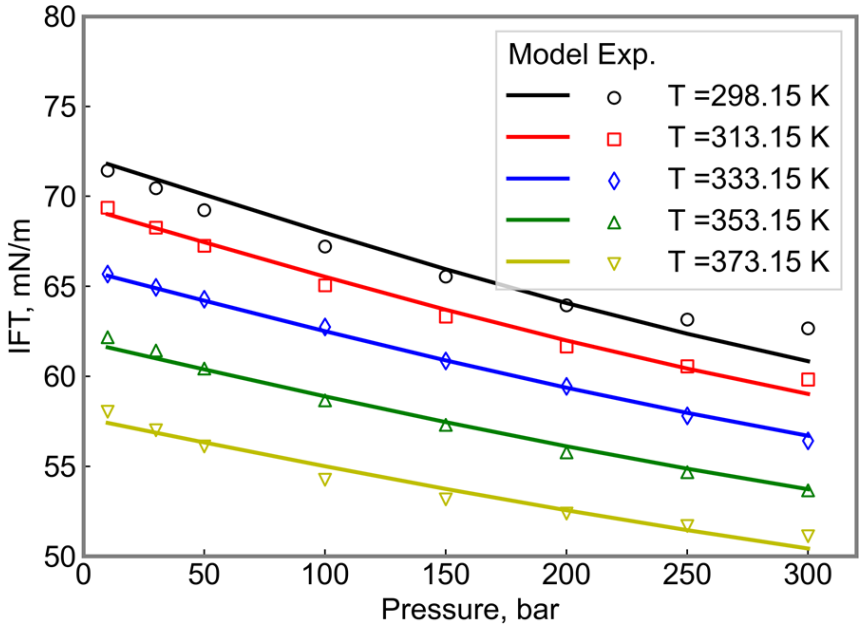

Fig. 3—Calibrated Parachor model for IFT of water and N_2 at various temperatures and pressures. Experimental data (Yan et al. 2001) are shown by black circles at 298.15 K, red squares at 313.15 K, blue diamonds at 333.15 K, green triangles at 353.15 K, and yellow downward triangles at 373.15 K.

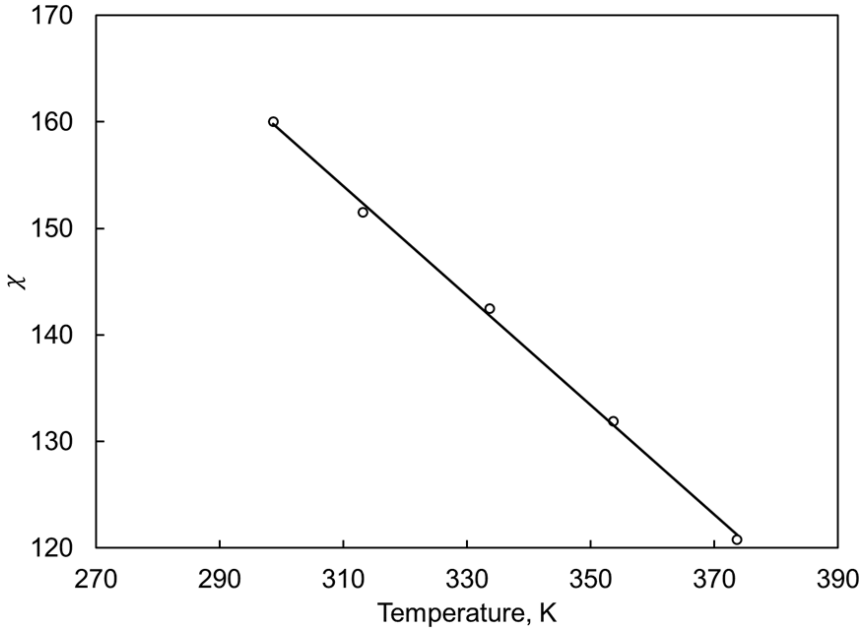

Fig. 4—Temperature-dependent coefficient χ for the modified Parachor model in this research.

$$F_i = \ln f_{iV} - \ln f_{iL} = 0, \tag{36}$$

and the capillary pressure equation

$$F_{N_C+1} = P_V - P_L - P_{\text{cap}} = 0. \tag{37}$$

The NR algorithm uses the number of moles and total volume of the vapor phase as the independent variables.

Each SS iteration contains two main steps—the composition update and the volume update. The composition update is based on the traditional method of Rachford and Rice that solves the material balance for $\ln K_i$

$$\ln K_i = \ln x_{iV} - \ln x_{iL}. \tag{38}$$

The Rachford-Rice routine used in this research is described in Okuno et al. (2010). The volumes are updated through the solution of the pressure equation, subject to the volume balance.

A concise description of the sequential iteration scheme for the SS algorithm is presented below, and Appendix B shows a flow chart of the algorithm.

Step 1. Initialize ln K and V. Use the stability analysis (Achour and Okuno 2020) if the reference phase is intrinsically stable; otherwise, use Wilson's correlation at the specified total molar volume. Initialize the iteration index k: $k \leftarrow 1$.

Step 2. If $\max_{i<N_C}\{|F_i|\} > \varepsilon_{\mathrm{NR}}$, switch to the NR algorithm.

Step 3. Compute $\ln P\varphi_L^k$, $\ln P\varphi_V^k$, and the SS under-relaxation factor ζ_{SS}^k.

Step 4. Update the capillary pressure using under-relaxation based on the capillary pressure model P_C^k evaluated at composition $\mathbf{x}_L^{k-1}$ and $\mathbf{x}_V^{k-1}$ and molar volumes $\underline{V}_L^{k-1}$ and $\underline{V}_V^{k-1}$.

$$P_C^k \leftarrow \left(1-\zeta_{\mathrm{SS}}\right)P_C^{k-1} + \zeta_{\mathrm{SS}}\mathcal{P}_C^k.$$

Step 5. Update the phase compositions.

5.1 Update ln K by using an SS step

$$\ln K_i^k \leftarrow \left(1-\zeta_{\mathrm{SS}}\right)\ln K_i^{k-1} + \zeta_{\mathrm{SS}}\left(\ln\phi_{iL}P_L - \ln\phi_{iV}P_V\right), \text{ where } i = 1,\ldots,N_C.$$

5.2 Solve the Rachford-Rice equations for the phase compositions $\mathbf{x}_L^k$ and $\mathbf{x}_V^k$, and the phase molar fractions β_L^k and β_V^k.

Step 6. Update the phase molar volumes by solving Eq. 13 using Newton's method.

Step 7. If the lower-pressure phase is intrinsically unstable, then use bisection to reduce its molar volume until it lies on the limit of intrinsic stability (spinodal boundary).

Step 8. Check for convergence. If $\max_{i\le N_C}\{|F_i|\} < \varepsilon_F$, then stop. Otherwise, $k \leftarrow k+1$ and return to Step 2. In this research, ε_F is set to 10^{-10}.

In Step 2, the switching criterion from SS to NR $\max_{i<N_C}\{|F_i|\} > \varepsilon_{\mathrm{NR}}$ is evaluated. The SS algorithm can converge to the solution without switching to the NR method when $\varepsilon_{\mathrm{NR}}$ is set to a value lower than that of $\varepsilon_{\mathrm{SS}}$. A description of the sequential iteration scheme is presented below for when the switching criterion is satisfied and the NR algorithm is activated. The specific expressions for computing the Jacobian $\mathcal{J}^k$ for both the definite and indefinite solution are given in Achour (2023).

Step 3. Compute the gradient F^k and the Jacobian $\mathcal{J}^k$.

Step 4. Solve for the Newton direction $\Delta\mathbf{v}_L^k$ from equation $\mathcal{J}^k\left(\Delta\mathbf{v}_L^k\right) = \mathbf{F}^k$.

Step 5. Compute the under-relaxation factor ζ_{NR} necessary to enforce the feasibility constraint Eqs. 14 and 15.

Step 6. Update the number of moles and volume of the vapor phase $\mathbf{v}_V^{k+1} \leftarrow \mathbf{v}_V^k - \zeta_{\mathrm{NR}}\Delta\mathbf{v}_L^k$ and the liquid phase $\mathbf{v}_L^{k+1} \leftarrow \mathbf{v}_L^k + \zeta_{\mathrm{NR}}\Delta\mathbf{v}_L^k$.

Step 7. Check for convergence. If $\max_{i\le N_C}\{|F_i|\} < \varepsilon_F$, then stop. Otherwise, $k \leftarrow k+1$ and return to Step 3. In this research, ε_F is set to 10^{-10}.

Initial Guess. Raoult's law does not give accurate K values as the initial guesses for stability and phase-split calculation in this research. Also, N_2 and water are strongly immiscible; therefore, a specific initial estimation for K values is possible as presented in this subsection. Let us define the index $i = 1$ as the component index for water. To search for an incipient aqueous phase, an initial guess for the composition is $x_i = 10^{-9}$, for $i = 2, \ldots, N_C$ and $x_1 = 1.0 - (N_C - 1) \times 10^{-9}$. The molar volume is set to

$$\underline{V} = \max\left(18\times10^{-6}, 1 + 10^{-4}b\left(\mathbf{x}\right)\right), \tag{39}$$

to search for an incipient aqueous phase. To search for an incipient vapor phase, an initial guess for the composition is $x_i = z_i/t$ for $i = 2, \ldots, N_C$ and $x_1 = 10^{-9}/t$, where $t = 10^{-9} + \sum_{j=2}^{N_C} z_j$. The molar volume is set to

$$\underline{V} = \underline{V}_{\mathrm{total}}/\left(1.0 - z_1\right), \tag{40}$$

to search for an incipient vapor phase.

The initial guess composition for the phase-split calculation is the same as that described in Achour and Okuno (2021) if the Hessian of the reduced Helmholtz free energy is positive definite. However, the molar volumes are initialized by solving $\underline{V} = \beta_L\underline{V}_L + \beta_V\underline{V}_V$ subject to $P_L = P_V$ using a NR algorithm. The algorithm is as follows:

Step 1. Set $P^k \leftarrow 10$ bar and $k \leftarrow 1$, $P_{\min} \leftarrow 10^{-9}$, $P_{\max} \leftarrow 2\times10^{-9}$.

Step 2. Solve the EOS for the molar volume of liquid $\underline{V}_L$ and vapor $\underline{V}_V$ at the pressure P^k and compute the derivative of pressure with volume for both phases. Compute the total volume $V_t = V_L + V_V$.

If $V_t < V_{\mathrm{total}}$, set $P_{\max} \leftarrow P^k$. Otherwise, set $P_{\min} \leftarrow P^k$.

Step 3. Update the pressure

$$P^{k+1} \leftarrow P^k - \frac{V_t - V_{\mathrm{total}}}{\frac{\partial V_L}{\partial P} + \frac{\partial V_V}{\partial P}}.$$

If $\left|V_t - V_{\mathrm{total}}\right|/V_{\mathrm{total}} < 10^{-7}$, the algorithm is converged. Use the liquid- and vapor-phase compositions and volumes as the initial guess to the flash calculation. Otherwise, set $k \leftarrow k+1$ and return to Step 2.

If the Hessian of the reduced Helmholtz free energy is not positive definite, it is unconditionally unstable. The L-phase mole fraction and initial guess compositions are set as follows:

$$\beta_L \leftarrow 10^{-5}\sum_{j=2}^{N_C} x_i + \left(1-10^{-5}\right)x_1,\ x_{iL} \leftarrow \frac{10^{-5}x_i}{\beta_L},\ \text{where } i = 2,\ldots,N_C,\ \text{and}$$

$$x_{1L} \leftarrow \frac{\left(1-10^{-5}\right)x_1}{\beta_L}.$$

The V-phase mole fraction and initial guess compositions are set as follows:

$$\beta_V \leftarrow \left(1-10^{-5}\right)\sum_{j=2}^{N_c} x_i + 10^{-5}x_1,\ x_{iV} = \frac{\left(1-10^{-5}\right)x_i}{\beta_V},\ \text{where } i = 2,\ldots,N_c,\ \text{and}$$

$$x_{1V} = \frac{10^{-5}x_1}{\beta_V}.$$

The volumes of both phases are then computed using the NR algorithm above.

Application of the Thermodynamic Equilibrium Model to Aqueous NB Fluid with N_2

This section first describes experiments and their results for aqueous NB fluids with N_2 and then presents the application of the thermodynamic equilibrium model to analyze the data.

Generation of Aqueous NB Dispersion of N_2 at Elevated Pressures. Fig. 5 shows a schematic for the experiment to generate aqueous NB fluid in this research. Deionized water and high-purity N_2 gas were pressurized in accumulators equipped with a piston. They were coinjected at an equal volumetric rate of 50 cm^3/h (in total, 100 cm^3/h) at the test pressure into a core holder in which three porous stainless-steel membranes are placed. The confining pressure on the core holder was greater than the test pressure by 35 bar. Each membrane had a diameter of 25.4 mm and a thickness of 3 mm with homogeneous pores of 5 μm. One possible mechanism for such a porous membrane to generate aqueous NB dispersion is that as the water and gas flow through the pores, the hydrodynamic mixing and gas snap-off make dispersed gas bubbles in the aqueous phase that are supersaturated by the gas component. The water exiting from these three membranes contains a greater amount of N_2 than the inherent solubility because of two modes of dispersion—bubble dispersion in the internal phase and molecule dispersion in the external phase. The aqueous NB fluid prepared was then transferred into a receiver accumulator for storage at high pressure.

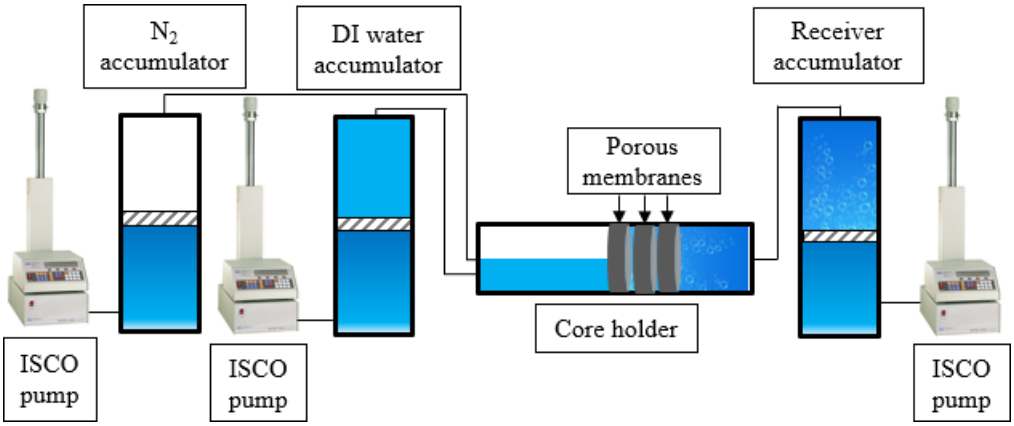

Fig. 5—Schematic of the experimental setup used to generate aqueous NB fluid.

Fig. 6 shows a schematic for the experiment to measure the thermodynamic properties of an aqueous NB fluid. Following the procedure given previously, the aqueous NB fluid sample was transferred from the receiver accumulator into a sapphire cell at pressure P_1. The sapphire cell provides a viewing window to observe the behavior of the aqueous NB fluid, and it can withstand pressures up to 350 bar. The volume of the sapphire cell is known and denoted as V_{cell}. The cell was connected to the top side of an accumulator containing a piston and a pressure gauge. The piston was initially set at the top of the accumulator, and the dead volumes (V_d) in the line connecting the sapphire cell to the accumulator, as well as the line connecting the accumulator to the pressure gauge, were evacuated. Next, the cell was gradually depressurized by opening the cell to fill the dead volumes with N_2 from the aqueous NB fluid. The bottom side of the accumulator was then opened to the atmosphere. Water was collected to gauge the displacement of the piston as the aqueous NB fluid sample was depressurized or expanded. The water collected corresponds to the volume of depressurized N_2 in the aqueous NB fluid. The mass of the water collected is denoted as m_{w2}, and the pressure at the top side of the accumulator after depressurization is P_2. Finally, the remaining water in the cell was collected and its mass m_{w3} was measured.

These experiments were performed in Austin, Texas, USA, during the week of 3 April 2023. According to timeanddate.com (2023), the average atmospheric pressure was 1.0135 bar during this period with a minimum of 1.000 bar and a maximum of 1.026 bar in Austin, Texas, USA. This pressure was used as P_3 in the calculation. The temperature was recorded at 295.15 K for each measurement.

Analysis of Aqueous NB Fluid with N_2. This subsection first shows the application of the thermodynamic framework described earlier to analyze the experimental data for aqueous NB fluid with N_2 and to calculate the apparent radius of bubbles for each aqueous NB fluid sample. Although size distributions of NBs have been measured and reported for low-pressure (mostly atmospheric pressure) samples in the literature by using light scattering, spectral, and high-resolution imaging techniques, such measurement for high-pressure aqueous NB samples is not an easy task, requiring a specific design for the high-pressure sample container used. The estimated bubble sizes in this section enable us to understand the overall behavior of the aqueous NB fluid with N_2 from a thermodynamic viewpoint.

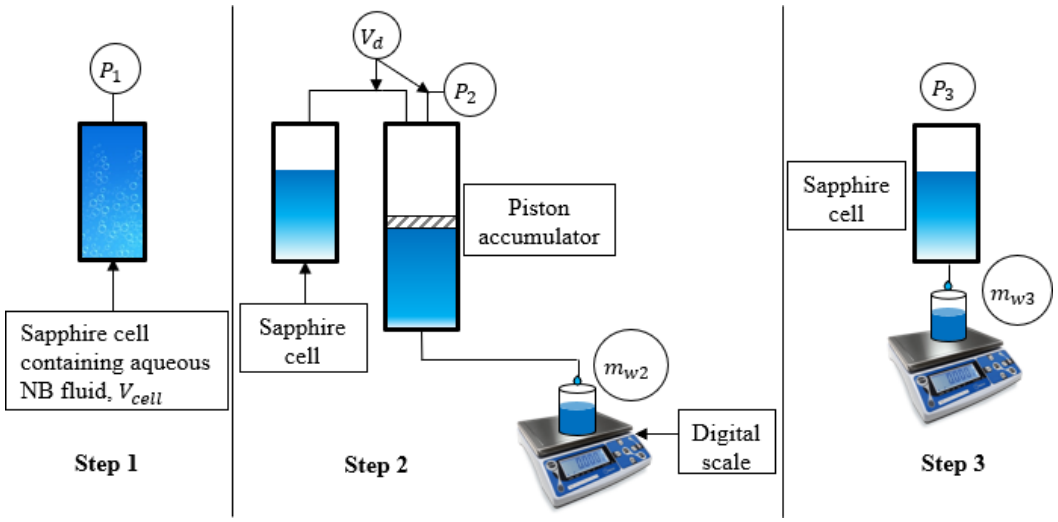

Fig. 6—Schematic of the experimental setup to measure the thermodynamic properties of the aqueous NB fluid. The background image for bubbled water was retrieved from freepik.com.

First, the data are analyzed by using the thermodynamic equilibrium model based on the following assumptions:

1. Data were measured at equilibrium.
2. The water mass measured in Step 3 **(Fig. 6)** was at equilibrium with the N_2 gas cap in the sapphire cell.
3. The mass of water left in the sapphire cell in the form of droplets on the interior was negligible in comparison to the mass measured as m_{w3}.
4. The system was closed in the depressurizing process from P_2 to P_3.

As explained in the section "Thermodynamic Stability and Equilibrium of Aqueous NB Fluid," the phase equilibrium including capillary pressure can be specified by $(N_C + 3)$ variables (e.g., temperature, total volume, total mole numbers of components, and capillary pressure) (Achour and Okuno 2020). Here, we use the thermodynamic model for temperature, total volume, total mole numbers of components, and the external phase pressure, which are measurable (directly or indirectly) for aqueous NB fluid samples in this research.

The procedure below first explains how to estimate the total mole numbers in the sapphire cell in Step 1 of the experiment **(Fig. 6)** and then how to determine the apparent radius of bubbles for the external phase pressure P_1.

- Perform a flash calculation at P_3 (atmospheric pressure) and 295.15 K for an equimolar mixture of the water/N_2 binary system. The mixture is assumed to be equimolar only to obtain the equilibrium aqueous-phase composition in Step 3. The volume of the aqueous phase is calculated as $V_{w3} = m_{w3}\underline{V_L}/M_L$, where $\underline{V_L}$ and M_L are the equilibrium aqueous-phase molar volume and weight. The mole number for water in the aqueous phase is $n_{w3} = m_{w3}/M_L = d_{1L}V_{w3}$.
- Perform a flash calculation at P_2 and 295.15 K. The total volume of the aqueous phase in Step 2 is $V_{L2} = n_{w3}/d_{1L}$, where d_{1L} is the water molar density in the aqueous phase obtained.
- Perform a flash calculation at P_3 and 295.15 K for a binary water/N_2 mixture where N_2 (as an approximate composition of air) is at equilibrium with the water collected in Step 2. The volume of water collected is therefore $V_{w2} = m_{w2}\underline{V_L}/M_L$, where $\underline{V_L}$ and M_L are the equilibrium aqueous-phase molar volume and weight. The total volume of the mixture at P_2 is therefore $V_{t2} = V_{\text{cell}} + V_{w2} + V_d$, where V_d is the dead volume contained in the line connecting the sapphire cell and the accumulator and the line connecting the accumulator to the pressure gauge.
- Determine the total number of moles in the system between the sapphire cell and the accumulator, which gives the liquid volume V_{L2} and the gas volume $V_{t2} - V_{L2}$.
- Perform flash calculations at the total volume V_{cell} and the mole numbers of water and N_2 with a bubble radius of 1 nm and 104 nm. If the external phase pressure P_1 lies between the values for 1 nm and 104 nm, perform a bisection to find the bubble radius that gives the external phase pressure P_1.

Table 9 shows the data measured in the experiment for aqueous NB fluids with N_2. Use of the data in **Table 9** with the procedure given above yielded a possible radius of bubbles for the temperature (295.15 K), total volume (V_{cell}), mole numbers for water (n_w) and N_2 (n_{N_2}), and external phase pressure (P_1). Among these input parameters, m_{w3} was the most uncertain and found to be influential to the resulting bubble radius in the calculation because the density of water was much greater than that of nitrogen. **Table 9** shows that the uncertainty of m_{w3} was ±3 g; for example, if m_{w3} was smaller by 0.1 g, it could increase the calculated apparent radius of bubbles by one order of magnitude. Therefore, it was not possible to quantitatively determine the apparent radius of bubbles for these data with an order-of-magnitude accuracy only by using thermodynamic calculation. Nonetheless, the existence of bubbles with a realistic apparent radius for the actual experimental conditions indicates the possibility of thermodynamic aqueous NB fluid, in which the gaseous component is dispersed molecularly and also as bubbles in the external aqueous phase with capillary pressure.

To analyze the experimental data, the thermodynamic equilibrium model was solved for the overall composition of the water/N_2 binary system at the specified temperature, the total molar volume, and the bubble radius. Because the mass of water collected from the sapphire cell m_{w3} was relatively uncertain, the thermodynamic calculation was repeated for multiple values of m_{w3} for each experiment within the range of possible values as shown in **Table 9**. For each calculation, the mole number for water n_w and the L-phase volume were adjusted based on m_{w3}. The mole number for nitrogen n_{N_2} was based on the V-phase volume in Step 2, using the mass of water collected from the receiver accumulator m_{w2} from **Table 9**. The radius of bubbles was then determined for a system specified at fixed T, n_{N_2}, n_w, V_{cell}, and P_L.

Fig. 7 shows the overall N_2 mole fraction z_{N_2} with a bold black line, the mole fraction of N_2 in the aqueous phase $x_{N_2,W}$ with a black dashed line, and that in the absence of capillary pressure $x_{N_2,W}\left(P_C = 0\right)$ with a dotted line for varying radius of bubbles. The stability criterion C $(= D - \varepsilon$ see Eq. 21) was plotted for the secondary y-axis with a black dash-dotted line. The radius of bubbles at which $C = 0$

Parameter	P_1	P_2	P_3	m_{w2}	m_{w3}	V_{cell}	V_d
Unit	bar	bar	bar	g	g	mL	mL
Exp. 1	34.59	1.22	1.013	4.54	10.765 ± 3	13.69	6.705
Exp. 2	68.93	1.29	1.013	11.4	10.930 ± 3	13.69	6.705
Exp. 3	104.2	1.15	1.013	23.58	11.405 ± 3	13.69	6.705
Exp. 4	103.3	1.29	1.013	19.49	11.310 ± 3	13.69	6.705
Exp. 5	103.4	1.29	1.013	21.22	11.295 ± 3	13.69	6.705
Exp. 6	138.2	1.22	1.013	32.01	11.040 ± 3	13.69	6.705
Exp. 7	207.8	1.22	1.013	57.41	11.835 ± 3	13.69	6.705
Exp. 8	277.1	1.22	1.013	71.92	12.040 ± 3	13.69	6.705

Table 9—Experimental data used in the calculation of aqueous NB of N_2 at 295.15 K.

was the minimum radius that met the stability criterion. The minimum radius of bubbles was calculated as 60.8 nm for **Fig. 7a** (Exp. 1 at 34.59 bar), 39.1 nm for **Fig. 7b** (Exp. 2 at 68.93 bar), 25.4 nm for **Fig. 7c** (Exp. 3 at 104.2 bar), 27.0 nm for **Fig. 7d** (Exp. 4 at 103.3 bar), 23.3 nm for **Fig. 7e** (Exp. 5 at 103.4 bar), 16.5 nm for **Fig. 7f** (Exp. 6 at 138.2 bar), 8.54 nm for **Fig. 7g** (Exp. 7 at 207.8 bar), and 7.14 nm for **Fig. 7h** (Exp. 8 at 277.1 bar). **Table 10** presents n_{N_2} and n_w and the respective mass of N_2 and water used for the calculations with the data sets Exps. 1–8.

Parameter	r	n_{N_2}	n_w	m_{N_2}	m_w
Unit	nm	mol	mol	g	g
Exp. 1	60.18	0.5594	0.7572	0.01567	13.64
Exp. 2	39.00	0.9447	0.7580	0.02646	13.66
Exp. 3	25.33	1.401	0.7583	0.03924	13.66
Exp. 4	26.98	1.362	0.7584	0.03814	13.66
Exp. 5	23.21	1.451	0.7581	0.04065	13.66
Exp. 6	16.52	1.898	0.7586	0.05316	13.67
Exp. 7	8.542	3.136	0.7583	0.08785	13.66
Exp. 8	7.147	3.843	0.7594	0.1076	13.68

Table 10—Bubble radii, component moles, and mass at $C = 0$ for each experiment at 295.15 K and a volume of 13.69 mL.

Fig. 8 shows the total reduced Helmholtz free energy using a bold black line and the total Helmholtz free energy of the vapor phase and the interface plotted for the secondary y-axis using a dotted line. For all the experimental data, the free energies monotonically decrease with decreasing bubble radii. That is, the overall composition that corresponds to $C = 0$ results in the smallest possible Helmholtz free energy of the aqueous NB fluid with N_2 for a given temperature, total molar volume, and external phase pressure based on the thermodynamic equilibrium model and the experimental data in this research.

To give an overview of the calculated properties of the aqueous NB fluid samples in this research, an apparent radius of bubbles was calculated for the overall composition that corresponds to $C = 0$ for each pressure for each aqueous NB fluid sample by using the thermodynamic equilibrium model. Once a radius of bubbles is set, the model gives various equilibrium properties of the aqueous NB fluid samples, which is an important benefit of using a thermodynamic model in this research. **Fig. 9a** shows that the mass of water m_{w3} used for calculation at each pressure is within the uncertainty as given in **Table 9. Fig. 9** also shows bubble radius, bubble number density, the amount of N_2 in the bubbles, and the amount of N_2 that is molecularly dissolved in the external aqueous phase, total interfacial area, IFT, and capillary pressure with respect to the external (aqueous) phase pressure (P_L). The N_2 contents in **Fig. 9d** were calculated as $x_{N_2V}\beta_V$ for the gas and $x_{N_2L}\beta_L$ for the liquid water phase, where β_V is the vapor-phase mole fraction (as a total of bubbles) and β_L is the aqueous-phase mole fraction. The dotted line denoted as "Saturation" represents $x_{N_2L}\beta_L$ when the N_2 and water are at equilibrium with no bubbles and therefore with a single planar interface between two bulk phases in the system. **Fig. 9e** shows the fraction of N_2 contained in bubbles calculated as $x_{N_2V}\beta_V/z_{N_2}$. The error bars are determined as half the difference between the smallest and largest values at 104 bar since the experiment was repeated three times as Exps. 3, 4, and 5.

Figs. 9b and 9c show that the calculated radius decreased, and the number density of bubbles increased with increasing P_L. The extrapolation to atmospheric pressure using the two data points at the lowest pressure yields a bubble radius of 80 nm. This extrapolated radius lies within the range of measured bubble radii (25–200 nm) at atmospheric pressure (Alheshibri et al. 2016; Zhou et al. 2021).

Figs. 9d and 9e show that a large fraction of the N_2 in the system is molecularly dissolved in the external aqueous phase. This is one of the most important findings in this research; that is, the existence of bubbles increases the N_2 content in the system by increasing the molecule dispersion (supersaturation) in the aqueous phase much more than by containing N_2 as bubbles. The presence of bubbles in aqueous NB fluid at equilibrium tends to increase the level of supersaturation in the external aqueous phase with capillary pressure. The results indicate that this supersaturation is the main contributor to the amount of N_2 in the aqueous NB fluid. Because the gas content is one of the most fundamental properties of aqueous NB fluid (Ward et al. 1982), this insight gained by the thermodynamic equilibrium

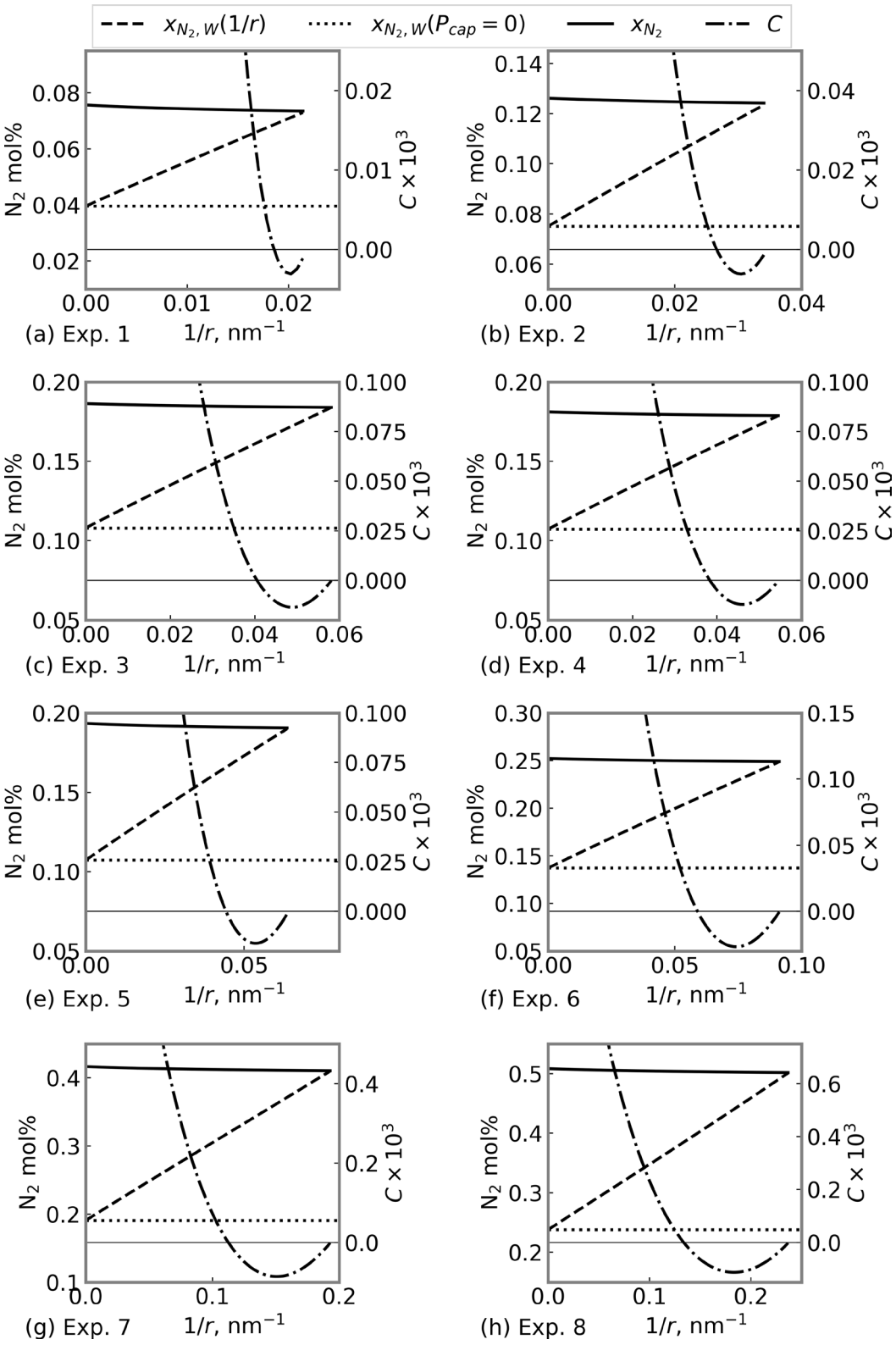

Fig. 7—Solutions of the thermodynamic equilibrium model for the aqueous NB fluid samples for Exps. 1–8. The secondary *y*-axis is the stability criterion $C = D - \varepsilon - D - \varepsilon$ (see Eq. 21) multiplied by 10^3.

model in this research has fundamental impacts on the research and development of NB technologies, such as devices and applications to surface and subsurface processes.

Limitations of experimental techniques in fundamental research of aqueous NB fluids are known in the literature (e.g., Tan et al. 2020); for example, dynamic light scattering techniques are currently unavailable for measuring bubble size distributions for aqueous NB fluids at elevated pressures, to the best of our knowledge. This section showed that the bubble size estimation by using the thermodynamic model was sensitive to the experimentally obtained mole numbers of components in the system; therefore, such dynamic light scattering

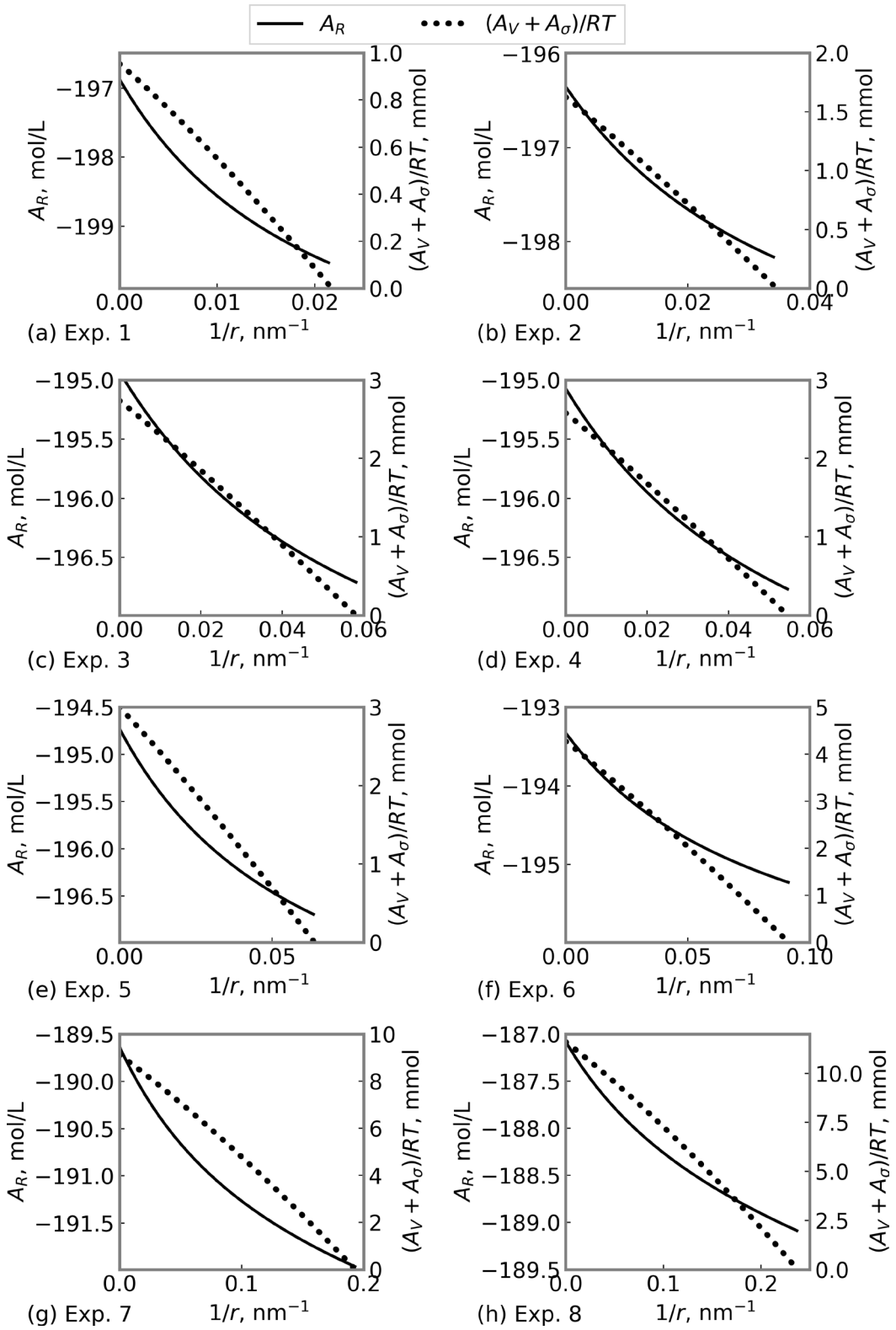

Fig. 8—Reduced total Helmholtz free energies [A_R and $(A_V + A_\sigma)/RT$] for the aqueous NB fluids with N_2 at 295.15 K for Exp. 1 through Exp. 8.

techniques, experimental data (gas content for a set of thermodynamic conditions), and thermodynamic models would be complementary for high-pressure applications of aqueous NB fluids.

One of the limitations of the models presented in this paper is that the IFT model neglected the dependency on the radius of curvature in the functional form of Eq. 34. Although **Fig. 9** presents the size-dependent IFT because of the thermodynamic relationships among variables, such as phase compositions, pressures, surface area, and IFT , Eq. 34 contains an obvious simplification; that is, the Parachor parameters calibrated for experiments on interfaces with much greater curvatures were applied for N_2 NB fluids at high pressures. A potential and practical way to improve the simplification is to apply a correction factor for interfacial curvature in Eq. 34 (Ono and Kondo

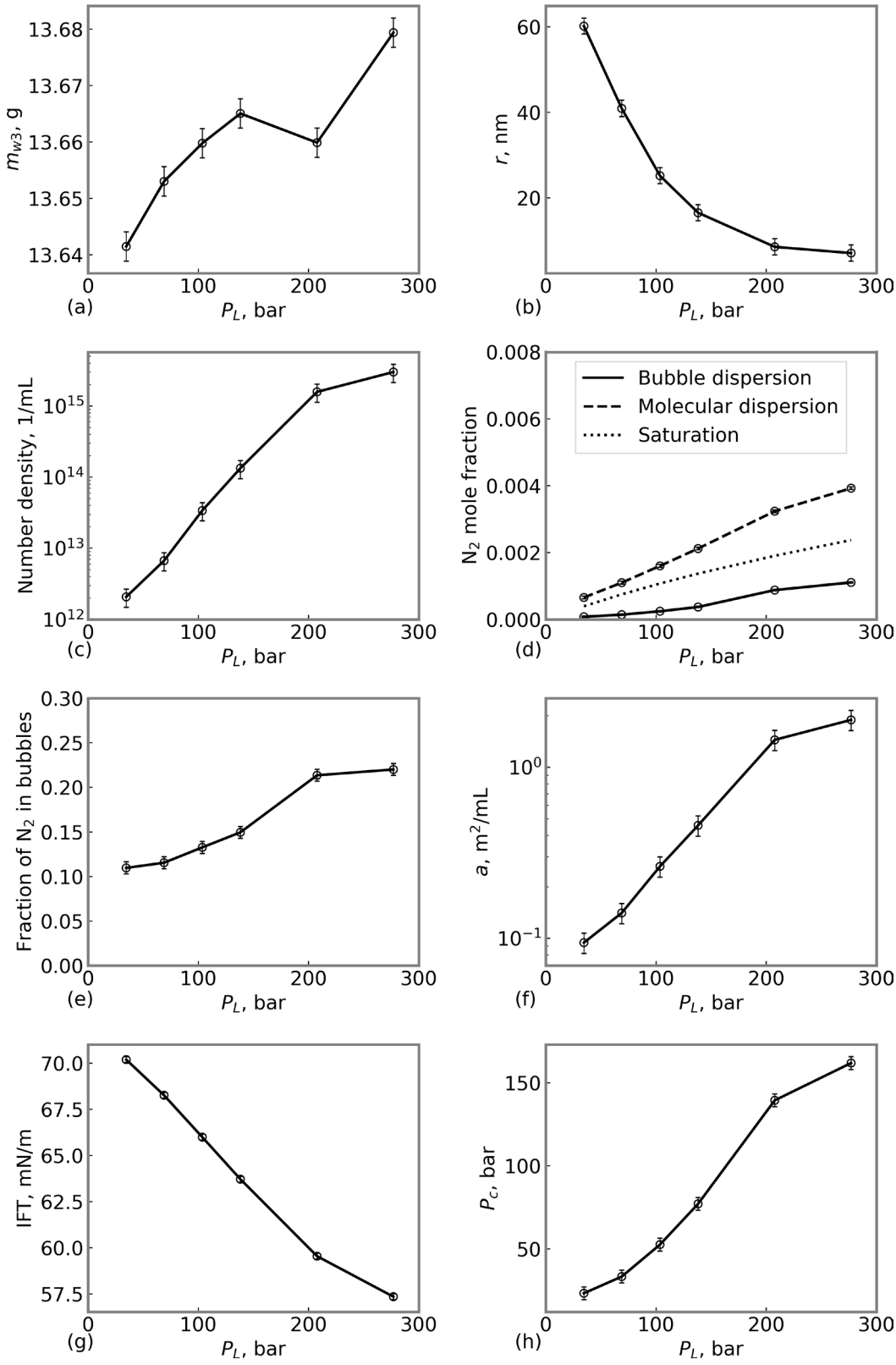

Fig. 9—Mass of water in the sapphire cell, bubble radius, bubble number density, N_2 content, fraction of N_2 in bubbles, interfacial area, IFT, and capillary pressure of N_2 in water for NB solutions at 295.15 K for Exp. 1 through Exp. 8.

1960; Santiso and Firoozabadi 2006; Firoozabadi 2016). Such improvements could be tested to evaluate the relative importance of phase composition and interface curvature to the magnitude of IFT; however, that is outside the scope of this paper.

Conclusions

This paper presented the thermodynamic equilibrium model for aqueous NB fluid using the GERG-2008 EOS. The model was applied to experimental data for an aqueous NB dispersion of N_2 at pressures up to 277 bara (4,019 psia) at 295.15 K (71.6°F). Thermodynamic analysis of the experimental data yielded the following conclusions:

- A thermodynamic system of aqueous NB fluid is possible if gas bubbles are dispersed in the external aqueous phase that is supersaturated by the gaseous species with no bulk gas phase. The energy analysis for aqueous NB fluid in this research indicates that the thermodynamic stability of aqueous NB fluid requires a minimum amount of gaseous species in the system.
- Application of the thermodynamic model to the high-pressure experimental data showed that the aqueous NB fluid system gives the smallest possible Helmholtz free energy at the overall composition that corresponds to the stable gas-bubble generation limit for a given temperature, total volume, and radius of bubbles.
- As the experimental data showed, the amount of gas in the aqueous NB fluid increased with increasing pressure of the external aqueous phase. Accordingly, the model indicated that the bubble radius decreased and the bubble number density increased with increasing pressure of the aqueous phase.
- The analysis of the data indicated that a large fraction (0.8–0.9) of the gaseous species (N_2) in the system was molecularly dissolved in the aqueous phase. Hence, the existence of bubbles was important to increase the level of N_2 supersaturation in the aqueous phase, but the amount of N_2 as bubbles was not the main contribution to the total amount of N_2 in the aqueous NB fluids in this research. However, this conclusion is subject to different levels of uncertainty in the models (i.e., IFT and EOS) and experimental data used in this research on high-pressure aqueous NB fluids.

Acknowledgments

This research was performed as part of the Energi Simulation Industrial Affiliate Program on Carbon Utilization and Storage (ES Carbon UT) at the University of Texas at Austin. Ryosuke Okuno holds the Pioneer Corporation Faculty Fellowship in the Hildebrand Department of Petroleum and Geosystems Engineering at the University of Texas at Austin.

References

Achour, S. H. 2023. *Modeling of Multiphase Multicomponent Transport in Tight Porous Media*. PhD Dissertation, The University of Texas at Austin.

Achour, S. H. and Okuno, R. 2020. Phase Stability Analysis for Tight Porous Media by Minimization of the Helmholtz Free Energy. *Fluid Phase Equilib* **520**: 112648. https://doi.org/10.1016/j.fluid.2020.112648.

Achour, S. H. and Okuno, R. 2021. Two-Phase Flash for Tight Porous Media by Minimization of the Helmholtz Free Energy. *Fluid Phase Equilib* **534**. https://doi.org/10.1016/j.fluid.2021.112960.

Alheshibri, M., Qian, J., Jehannin, M. et al. 2016. A History of Nanobubbles. *Langmuir* **32** (43): 11086–11100. https://doi.org/10.1021/acs.langmuir.6b02489.

Aursand, P., Gjennestad, M. A., Aursand, E. et al. 2016. The Spinodal of Single- and Multi-Component Fluids and Its Role in the Development of Modern Equations of State. *Fluid Phase Equilib* **436**: 98–112. https://doi.org/10.1016/j.fluid.2016.12.018.

Azevedo, A., Oliveira, H., and Rubio, J. 2019. Bulk Nanobubbles in the Mineral and Environmental Areas: Updating Research and Applications. *Adv Colloid Interface Sci* **271**: 101992. https://doi.org/10.1016/j.cis.2019.101992.

Favvas, E. P., Kyzas, G. Z., Efthimiadou, E. K. et al. 2021. Bulk Nanobubbles, Generation Methods and Potential Applications. *Curr Opin Colloid Interface Sci* **54**: 101455. https://doi.org/10.1016/j.cocis.2021.101455.

Fechter, T., Villablanca, R., Leontijevic, V. et al. 2023. Interfacial Tension of Water near to Critical Conditions by Using the Pendant Drop Method: New Experimental Data and a Correlation Based on the Parachor Method. *J Supercrit Fluids* **196**: 105899. https://doi.org/10.1016/j.supflu.2023.105899.

Firoozabadi, A. 2016. *Thermodynamics and Applications in Hydrocarbon Energy Production*. New York, USA: McGraw-Hill.

Gernert, J. and Span, R. 2016. EOS–CG: A Helmholtz Energy Mixture Model for Humid Gases and CCS Mixtures. *J Chem Thermodyn* **93**: 274–293. https://doi.org/10.1016/j.jct.2015.05.015.

Guo, B., Firoozabadi, A., Jackson, M. M. et al. 2023. Carbon Dioxide Viscosification by Polyolefins. US Patent Application US18/231,984.

Heidaryan, E., Robustillo Fuentes, M. D., and Pessôa Filho, P. de A. 2019. Equilibrium of Methane and Carbon Dioxide Hydrates Below the Freezing Point of Water: Literature Review and Modeling. *J Low Temp Phys* **194** (1–2): 27–45. https://doi.org/10.1007/s10909-018-2049-2.

Iguchi, M., Kaji, M., and Morita, Z.-I. 1998. Effects of Pore Diameter, Bath Surface Pressure, and Nozzle Diameter on the Bubble Formation from a Porous Nozzle. *Metall Mater Trans B* **29** (6): 1209–1218. https://doi.org/10.1007/s11663-998-0043-9.

Imre, A. R., Baranyai, A., Deiters, U. K. et al. 2013. Estimation of the Thermodynamic Limit of Overheating for Bulk Water from Interfacial Properties. *Int J Thermophys* **34** (11): 2053–2064. https://doi.org/10.1007/s10765-013-1518-8.

Jarrahian, A. and Nakhaee, A. 2019. Hydrate–Liquid–Vapor Equilibrium Condition of N2 + CO2 + H2O System: Measurement and Modeling. *Fuel* **237**: 769–774. https://doi.org/10.1016/j.fuel.2018.10.017.

Jin, J., Wang, R., Tang, J. et al. 2020. Dynamic Tracking of Bulk Nanobubbles from Microbubbles Shrinkage to Collapse. *Colloids Surf* **589**: 124430. https://doi.org/10.1016/j.colsurfa.2020.124430.

Kaptay, G. 2012. The Gibbs Equation versus the Kelvin and the Gibbs-Thomson Equations to Describe Nucleation and Equilibrium of Nano-Materials. *J Nanosci Nanotechnol* **12** (3): 2625–2633. https://doi.org/10.1166/jnn.2012.5774.

Kontogeorgis, G. M. and Folas, G. K. 2009. *Thermodynamic Models for Industrial Applications: From Classical and Advanced Mixing Rules to Association Theories*. New Jersey, USA: Wiley. https://doi.org/10.1002/9780470747537.

Kunz, O. and Wagner, W. 2012. The GERG-2008 Wide-Range Equation of State for Natural Gases and Other Mixtures: An Expansion of GERG-2004. *J Chem Eng Data* **57** (11): 3032–3091. https://doi.org/10.1021/je300655b.

Kunz, O., Klimeck, R., Wagner, W. et al. 2007. *The GERG-2004 Wide-Range Equation of State for Natural Gases and Other Mixtures*. Düsseldorf, Germany: VDI Verlag GmbH.

Kukizaki, M. and Goto, M. 2006. Size Control of Nanobubbles Generated from Shirasu-Porous-Glass (SPG) Membranes. *J Membr Sci* **281** (1–2): 386–396. https://doi.org/10.1016/j.memsci.2006.04.007.

Lawal, T., Argüelles-Vivas, F. J., Huh, C. et al. 2022. Properties of Gas-Containing Water. Paper presented at the 1st Annual Workshop (CarbonUT-1), the Energi Simulation Industrial Affiliate Program on Carbon Utilization and Storage, Austin, Texas, USA, 13–14 June.

Lemmon, E., Bell, I., Huber, M. et al. 2018. NIST Reference Fluid Thermodynamic and Transport Properties Database (REFPROP). *Version 10 - SRD*. https://doi.org/10.18434/T4/1502528.

Lemmon, E. W., Heinemann, V., Lu, J. et al. 2017. Version 2.0 of Routines for the Calculation of Thermodynamic Properties from the AGA 8 Part 2 GERG-2008 Equation of State. https://github.com/usnistgov/AGA8.

Li, X., Peng, B., Liu, Q. et al. 2023. Micro and Nanobubbles Technologies as A New Horizon for CO2-EOR and CO2 Geological Storage Techniques: A Review. *Fuel* **341**: 127661. https://doi.org/10.1016/j.fuel.2023.127661.
Maslennikova, V. Y. 1971. Solubility of Nitrogen in Water. *Tr. Gos. Nauchno-Issled. Proektn. Inst. Azotn. Prom-Sti. Prod. Org. Sint* **12**: 82–87.
Michelsen, M. L. 1982. The Isothermal Flash Problem. Part II. Phase-Split Calculation. *Fluid Phase Equilib* **9** (1): 21–40. https://doi.org/10.1016/0378-3812(82)85002-4.
Mikyška, J. and Firoozabadi, A. 2011. A New Thermodynamic Function for Phase-Splitting at Constant Temperature, Moles, and Volume. *AIChE J* **57** (7): 1897–1904. https://doi.org/10.1002/aic.12387.
Moortgat, J. and Firoozabadi, A. 2023. Viscosification of CO2 to Improve Subsurface Storage — A Modeling Study. *Int J Greenh Gas Control* **129**: 103984. https://doi.org/10.1016/j.ijggc.2023.103984.
Oellrich, L. R. and Althaus, K. 2004. GERG-Water Correlation: Relationship between Water Content and Water Dew Point Keeping in Consideration the Gas Composition in the Field of Natural Gas [GERG Technical Monograph 14].
Ohgaki, K., Khanh, N. Q., Joden, Y. et al. 2010. Physicochemical Approach to Nanobubble Solutions. *Chem Eng Sci* **65** (3): 1296–1300. https://doi.org/10.1016/j.ces.2009.10.003.
Okuno, R., Johns, R. T., and Sepehrnoori, K. 2010. A New Algorithm for Rachford-Rice for Multiphase Compositional Simulation. *SPE J.* **15** (2): 313–325. https://doi.org/10.2118/117752-PA.
Ono, S., Kondo, S. et al. 1960. Molecular Theory of Surface Tension in Liquids. In *Structure of Liquids*. Berlin, Heidelberg: Springer. https://doi.org/10.1007/978-3-642-45947-4.
Pal, N., Zhang, X., Ali, M. et al. 2022. Carbon Dioxide Thickening: A Review of Technological Aspects, Advances and Challenges for Oilfield Application. *Fuel* **315**. https://doi.org/10.1016/j.fuel.2021.122947.
Rigby, M. and Prausnitz, J. M. 1968. Solubility of Water in Compressed Nitrogen, Argon, and Methane. *The Journal of Physical Chemistry* **72** (1): 330–334. https://doi.org/10.1021/j100847a064.
Robinson, D. B. and Peng, D. Y., 1978. The Characterization of the Heptane and Heavier Fractions for GPA Peng-Robinson Programs. Gas Processors Association Research Report. Tulsa, Oklahoma.
Santiso, E. and Firoozabadi, A. 2006. Curvature Dependency of Surface Tension in Multicomponent Systems. *AIChE J* **52** (1): 311–322. https://doi.org/10.1002/aic.10588.
Schechter, D. S. and Guo, B. 1998. Parachors Based on Modern Physics and Their Uses in IFT Prediction of Reservoir Fluids. *SPE Res Eval & Eng* **1** (03): 207–217. https://doi.org/10.2118/30785-PA.
Snæbjörnsdóttir, S. Ó., Sigfússon, B., Marieni, C. et al. 2020. Carbon Dioxide Storage through Mineral Carbonation. *Nat Rev Earth Environ* **1** (2): 90–102. https://doi.org/10.1038/s43017-019-0011-8.
Tabasinejad, F., Moore, R. G., Mehta, S. A. et al. 2011. Water Solubility in Supercritical Methane, Nitrogen, and Carbon Dioxide: Measurement and Modeling from 422 to 483 K and Pressures from 3.6 to 134 MPa. *Ind Eng Chem Res* **50** (7): 4029–4041. https://doi.org/10.1021/ie101218k.
Tan, B. H., An, H., and Ohl, C.-D. 2020. How Bulk Nanobubbles Might Survive. *Phys Rev Lett* **124** (13). https://doi.org/10.1103/PhysRevLett.124.134503.
Terasaka, K., Yasui, K., Kanematsu, W. et al. 2021. *Ultrafine Bubbles*. New York: Jenny Stanford Publishing. https://doi.org/10.1201/9781003141952.
timeanddate.com. 2023. Past Weather in Austin, Texas, USA — Yesterday and Last 2 weeks. https://www.timeanddate.com/weather/usa/austin/historic.
Trædal, S., Stang, J. H. G., Snustad, I. et al. 2021. CO2 Liquefaction Close to the Triple Point Pressure. *Energies* **14** (24): 8220. https://doi.org/10.3390/en14248220.
Ulatowski, K., Sobieszuk, P., Mróz, A. et al. 2019. Stability of Nanobubbles Generated in Water Using Porous Membrane System. *Chem Eng Process: Process Intensif* **136**: 62–71. https://doi.org/10.1016/j.cep.2018.12.010.
Ushikubo, F. Y., Furukawa, T., Nakagawa, R. et al. 2010. Evidence of the Existence and the Stability of Nano-Bubbles in Water. *Colloids Surf A Physicochem Eng Asp* **361** (1–3): 31–37. https://doi.org/10.1016/j.colsurfa.2010.03.005.
Varzandeh, F., Stenby, E. H., and Yan, W. 2017. Comparison of GERG-2008 and Simpler EoS Models in Calculation of Phase Equilibrium and Physical Properties of Natural Gas Related Systems. *Fluid Phase Equilib* **434**: 21–43. https://doi.org/10.1016/j.fluid.2016.11.016.
Wang, H., Carrasco-Jaim, O., and Okuno, R. 2024. Aqueous Nanobubble Dispersion of CO_2 in Sodium Formate Solution for Enhanced CO_2 Mineralization Using Basaltic Rocks. Paper presented at the 2024 Carbon Capture, Utilization, and Storage Conference, Houston, Texas, USA, 11–13 March.
Wang, H., Lawal, T., Achour, S. H. et al. 2023. Aqueous Nanobubble Dispersion of CO_2 at Pressures Up To 208 Bara. *Energy Fuels* **37**: 19726–19737. https://doi.org/10.1021/acs.energyfuels.3c03660.
Ward, C. A., Tikuisis, P., and Venter, R. D. 1982. Stability of Bubbles in a Closed Volume of Liquid-Gas Solution. *J Appl Phys* **53** (9): 6076–6084. https://doi.org/10.1063/1.331559.
Weijs, J. H., Seddon, J. R. T., and Lohse, D. 2012. Diffusive Shielding Stabilizes Bulk Nanobubble Clusters. *Chemphyschem* **13** (8): 2197–2204. https://doi.org/10.1002/cphc.201100807.
Widiatmoko, P., Hendra Saputera, W., Devianto, H. et al. 2021. Effect of Bubble Size on Electrochemical Reduction of Carbon Dioxide to Formic Acid. *IOP Conf Ser: Mater Sci Eng* **1143** (1): 012001. https://doi.org/10.1088/1757-899X/1143/1/012001.
Yan, W., Zhao, G.-Y., Chen, G.-J. et al. 2001. Interfacial Tension of (Methane + Nitrogen) + Water and (Carbon Dioxide + Nitrogen) + Water Systems. *J Chem Eng Data* **46** (6): 1544–1548. https://doi.org/10.1021/je0101505.
Zhou, L., Wang, S., Zhang, L. et al. 2021. Generation and Stability of Bulk Nanobubbles: A Review and Perspective. *Curr Opin Colloid Interface* **53**: 101439. https://doi.org/10.1016/j.cocis.2021.101439.

Appendix A

Use of the PR EOS for Inherent Solubilities for the Water-N_2 Binary. This appendix presents the widely known challenges in using a cubic EOS for matching the inherent solubilities of water and gas. The PR EOS was used for the water-nitrogen binary system. The experimental data were taken from Tabasinejad et al. (2011). The EOS cannot match the solubility of nitrogen in the aqueous phase and that of water in the gaseous phase using a given value of the binary interaction parameter. This is an inherent limitation of a cubic EOS because its limited number of parameters do not give enough flexibility in matching data for relatively complex fluids involving polar species.

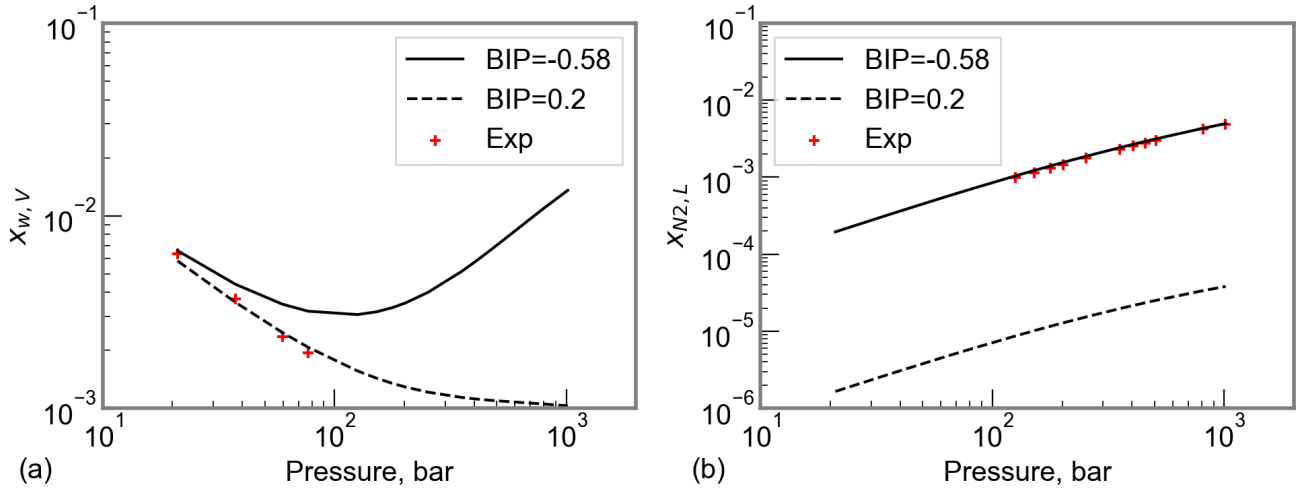

Fig. A-1—Comparison of the P-R EOS and experimental data for the solubility of water in the gaseous phase and that of N_2 in the aqueous phase at 323.15 K. The experimental data were taken from Tabasinejad et al. (2011). The EOS was able to match the solubility of nitrogen in the aqueous phase with a BIP value of −0.58 but deviated substantially from the solubility of water in the gaseous phase.

Appendix B

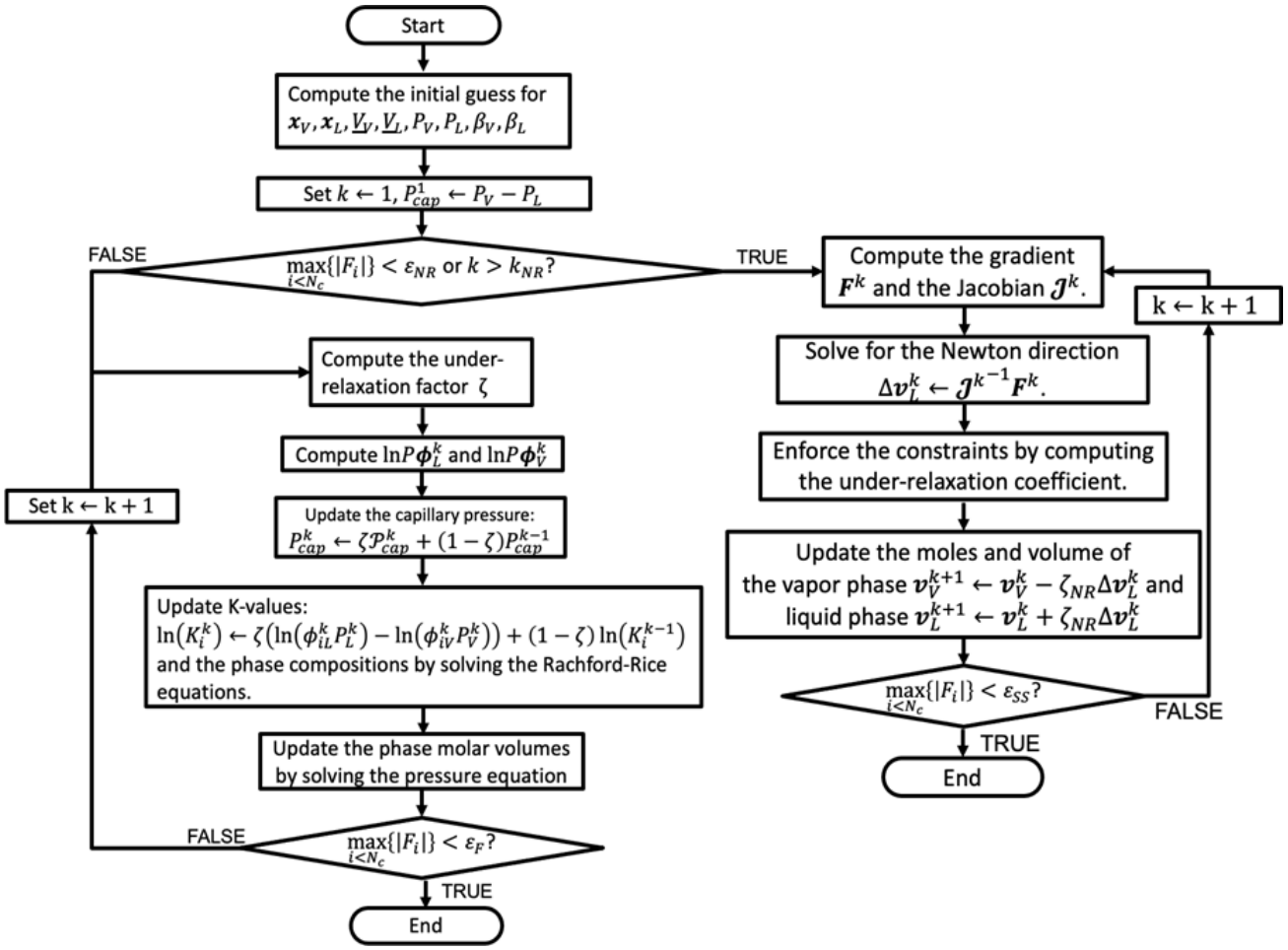

Fig. B-1—Flow chart for the flash calculation algorithm.